A Surface Study of the 1/1 Quasicrystal Approximant Ag-In-Gd

Gwyn Paul Evans
Supervisor: Prof. R .McGrath

Surface Science Research Centre
Department of Physics
The University of Liverpool

A Thesis Submitted for the Degree of
MPhys

May 2012

Abstract

Quasicrystal Approximants are fascinating alloy based materials, displaying the same large scale atomic clusters observed in related quasicrystalline phases, whilst maintaining a long range periodic order. Interesting in their own right, approximants are also useful in describing the atomic scale structure of their aperiodic parent quasicrystal. Surface studies of the 1/1 quasicrystal approximant Ag-In-Gd, grown in the (100) Miller plane, have been conducted. Low energy electron diffraction (LEED) and scanning tunneling microscopy (STM) used under ultra high vacuum (UHV), reveal facets orientated in the (310) plane adjacent to the (100). Analysis of STM and LEED data confirm the BCC lattice structure is decorated with large, icosahedral atomic clusters, centered upon each lattice point. Data suggests possible preservation of stable clusters upon the surface. Furthermore, evidence suggests the possibility that formation of certain terrace planes may be due to co-incidence with the icosahedral symmetry of the atomic clusters.

Acknowledgments

Firstly, I would like to thank Dr. H.R Sharma, Dr. J.A. Smerdon and Prof. R. McGrath for their time, guidance and supervision throughout the project within the Quasicrystal research group. I would also like to thank Thakur and Sanger for their continued discussion and willing assistance with my thesis project. Finally, I would like to thank my family and friends, who have offered their help and support throughout my studies.

1 Table of Contents

Project Summary: Motivation, Aims and Outcome

The 1/1 quasicrystal approximant Ag-In-Gd, has been studied using surface techniques under ultra high vacuum (UHV). The aim of the project was, in the first instance, to determine the optimum sample preparation parameters for this quasicrystal approximant. Following successful preparation, the surface structure of the sample was investigated using low energy electron diffraction (LEED) and scanning tunneling microscopy (STM). Finally comparisons with the theoretical bulk model for the approximant were made. The icosahedral quasicrystal (*i*-QC) systems consisting of Cd-RE (RE= Rare earth metals), whilst of great importance to the understanding of *i*-QC, cannot be studied under UHV conditions due to their low vaporization temperature at low pressure (1) (2).Thus, the *i*-Ag-In-RE systems of similar structure and properties, are used as a replacement for Cd in UHV surface study (3) (4). Therefore, motivations for studying the Ag-In-Gd approximant include the absence of previous surface characterization of this system and the opportunity to provide data to assist in the characterization of the parent quasicrystal surface. Approximants are suitable for comparison with parent quasicrystals as they typically form at similar compositions to those of quasicrystalline phases, provide a well defined starting point for models of the local atomic structure of quasicrystals and have similar physical properties (5). The project was successful in providing good data for comparison with theory and has led to some interesting conclusions concerning the structure of the surface. STM data confirms that icosahedral clusters are positioned upon lattice points throughout BCC structure of the Ag-In-Gd approximant. The data also suggests cluster preservation on the sample surface. Furthermore, it appears that the symmetry within the icosahedral clusters may have an impact upon the formation of surface structures, complimentary to the findings of Ph. Ebert *et al* (6). The evidence supporting this conclusion is outlined within this report, highlighting the need for future study of the Ag-In-Gd quasicrystal approximant. Table 3 in the appendix summarizes the measured experimental quantities.

1. Introduction

Classical crystals possess translational periodicity and display 1,2,3,4 and 6 fold symmetries (7). It was believed that 5 fold, 8-fold, 10-fold, and 12 fold rotational symmetries could not exist in crystalline condensed phases. This was in part due to the inability to tile the crystallographic plane using pentagonal, octagonal, decagonal or heptagonal shapes, without leaving gaps or overlaps throughout. Therefore, the creation of a stable structure using these symmetries was considered impossible, with a non-existent in nature (8). However, Shechtman, Blech, Gratias, and Cahn observed sharp diffraction patterns of icosahedral symmetry in Al-Mn alloy that was quenched rapidly from the melt (9). Crystals that display this characteristic, quasiperiodic translational order are now defined as "*quasicrystals*" (QC'S). They display two fundamental properties; long-range quasiperiodic translational order and long-range crystallographically forbidden orientation symmetry (8).

1.1 Physical Properties of Quasiperiodic Crystals

There are two classes of quasicrystals, one of which has periodicity in a single direction, whilst the other is completely a periodic (7). The former class are known as dihedral QCs, with the latter described as icosahedral QCs. The dihedral cases contain octagonal, decagonal, and dodecagonal QCs, which have 8-fold, 10-fold, and 12 fold axes, respectively. The Icosahedral class of QCs have six 5-fold, ten 3-fold, and fifteen 2-fold axes. (7 p. Chap2)

Quasicrystals consist of metallic elements, with a variety of metal based alloys displaying quasiperiodic structure. These include Al based transition metal alloys (e.g., A1Mn, AIMnSi, A1CuFe, and A1PdMn), alloys without transition metal elements displaying tetrahedrally closed-packed structures (FK alloys, e.g., A1-Cu-Li, Zn-Mg-RE (RE = rare earth)), and stable binary alloys (Cd alloys, e.g., $Cd_{5.7}$ Yb and $Cd_{17}Ca_3$). (10) .The distribution of known quasicrystals are shown in Figure 1:

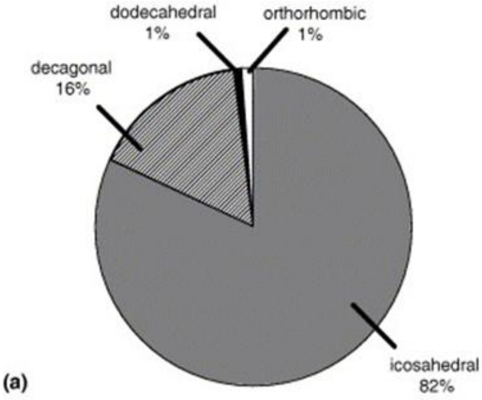

Figure 1: (a) the distribution of known quasicrystals (8)

QC's display many unusual properties that are unexpected for materials with metallic constituents (11). For example, they are relatively poor conductors of electricity, whilst the elements present in the alloy are excellent conductors. As the perfection of the quasicrystalline order increase, the conductivity drops. They also display a decrease in resistivity with increasing temperature and have an anomalously large resistivity at low temperature (12). QC's are extremely hard and brittle, strongly resisting deformation (7). Stable QCs are obtained by controlling the average number of the valence electrons per atom, (e/a) ≈ 2. Interestingly, the quasicrystalline structure are commonly among metallic alloys that display a ratio of (e/a) ≈2.

1.2 Quasiperiodicity, the Fibonacci Chain and the Golden Ratio

The quasiperiodicity seen in these metallic alloys can be described mathematically using the famous golden ratio and the Fibonacci chain (13). The golden ratio τ is an irrational number defined as:

$$\tau = \frac{1+\sqrt{5}}{2}$$

Equation 1: Golden Ratio (13)

An irrational number is one that cannot be expressed as a ratio of finite integers. The golden ratio is of relevance to the geometry of shapes that have five- fold symmetry, particularly to an icosahedron. For example the volume of an icosahedron is given by:

$$Volume = \frac{5\tau^5}{6}a$$

Equation 2: Volume of an Icosahedron (13)

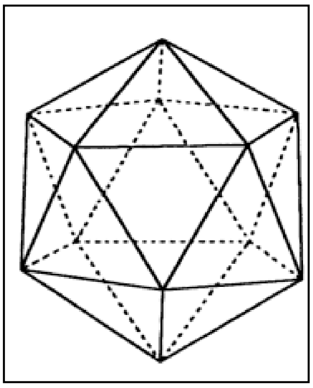

Figure 2: Icosahedron (13)

To show how the golden ratio can be used to construct a set of one dimensional, non-periodic lattice points, from two dimensional periodic lattice, the *"cut and project method"* is described:

"Starting with the square lattice in the plane, Z, a line with irrational slope, called E, is drawn, surrounded by a parallel strip of finite width. All lattice points inside the strip are then projected to E. If the slope is 1/τ, and the width of the strip coincides with the projection of a fundamental square to the internal direction $E_{int,}$ *we obtain what is called the Fibonacci chain*" (14)

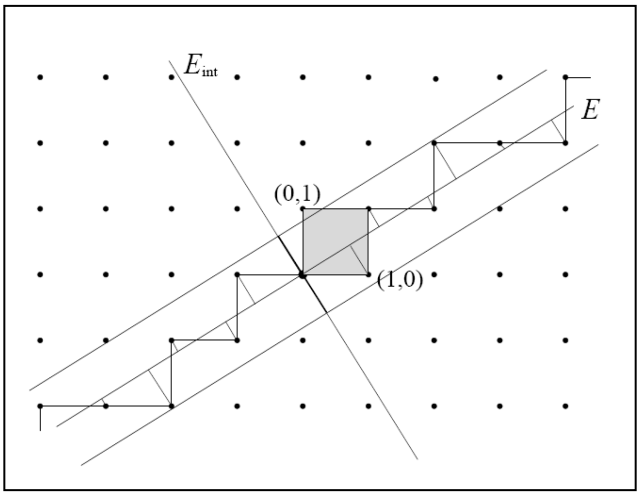

Figure 3: Cut and project method to construct a-periodic lattice point's (14)

The Fibonacci chain is a sequence of numbers in which the next number in the sequence is equal to the sum of the two previous. (14)

1, 1, 2, 3, 5, 8, 13, 21, 34, 55, 89, 144, 233, 377, ……

$$f_n = f_{n-1} + f_{n-2} \tag{15}$$

The successive ratio gives the golden ratio as *n* approaches infinity

$$\lim_{n\to\infty} \frac{f_{n+1}}{f_n} = \tau \tag{15}$$

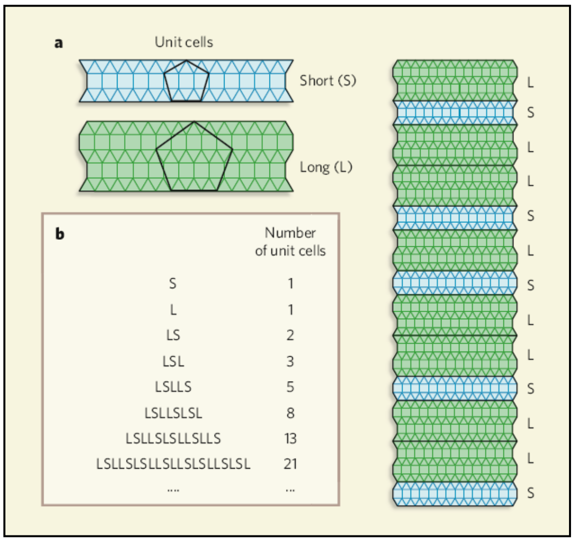

Figure 4: Quasiperiodic tiling structure based on the Fibonacci chain (16)

Figure 4 displays two unit cells of different width that stack up to form the pattern. The height of the cells corresponds to the heights of the small and large pentagons that have a size ratio equivalent to the golden mean. There is now a quasiperiodic sequence described by the Fibonacci chain, starting with one cell and expand using the sum of the two previous terms. (16). Using this two dimensional aperiodic tiling and certain matching rules, the entire two dimensional aperiodic plane can be filled with shapes of five-fold and 10-fold symmetry. This forms a mathematical basis upon which to base a structural model of quasicrystals. The main characteristics of a quasicrystal structure are understood as a combination of this quasiperiodic lattice and the clusters decorating it. The icosahedral class of QC contain clusters that consist of several tens of atoms, are arranged with approximate icosahedral symmetry (7)

1.3 Quasicrystal Approximants

An approximant is a material whose chemical composition and structural units are very similar to those of a quasicrystal, but still a classical crystal (5) (10). Many have identical atomic clusters spaced throughout their structure and have a large unit cell. An approximants’ space group is a subgroup of its corresponding quasicrystal. Therefore, the approximant can be generated by a rational cut through high-dimensional space, giving a relation between the structure of a quasicrystal and its approximant.

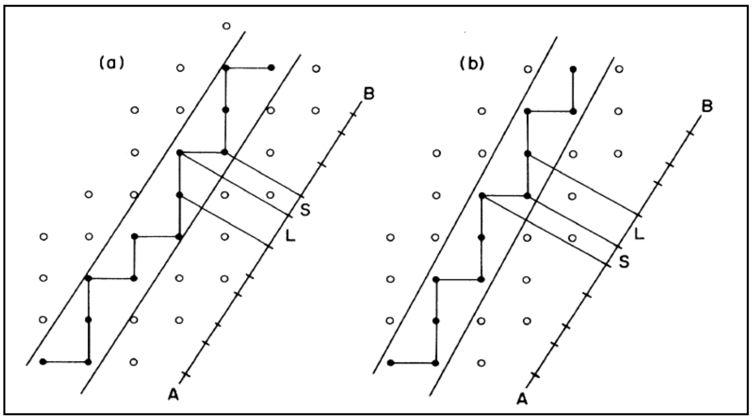

Figure 5: Construction of a quasiperiodic and approximant periodic lattice. (17)

A similar method to construct the lattice and show this relation is shown in Figure 5. It displays one dimensional tilings with long and short line segments. The tiling elements are generated by the projection of the edges of a two dimensional lattice, into a line AB with slope τ = $1+\sqrt{5}/2$. In (a), the selection of edges for projection is accomplished by choosing the gradient of the strip to be τ, as in the previous method for generating a quasiperiodic lattice. The strip in (b) has a gradient of 2/1, generating a periodic structure that is composed of the same tiling elements. By selecting the gradient of (b) to be a continued fraction approximate to τ, (e.g. gradient = 1/1, 2/1, 3/2, 5/3….where p/q are adjacent terms in the Fibonacci sequence), a structure with larger periods is created, which approximates the aperiodic tiling of a quasicrystal to a higher and higher degree of accuracy (17). In an icosahedral quasicrystal, identical icosahedral clusters exist in both the quasicrystal and the approximant but they are in quasiperiodic arrangement for the former and in a periodic arrangement for the latter. Approximants have played a crucial role in understanding the structures of quasicrystals since the structures of approximants have been well defined and described as local packings of icosahedral clusters. (7 p. Chap4 pg75). The Cd-Yb quasicrystal is a good example of a system in which the characterization of the quasicrystalline structure can be assisted using its crystalline approximant. However, Cd is not a suitable element for use in ultra high vacuum, as it evaporates upon heating (1) (18). Due to this, surface study of a surprisingly similar quasicrystalline phase of Ag-In-Yb was performed. As mentioned before, an important criterion for the formation of a quasicrystalline phase is the ratio of valance electrons per atom e/a (7 p. Chap4 Pg98). By replacing Cd with the Ag-In alloy, this ratio is preserved due to their relative atomic number, allowing the production of a similar quasicrystalline and approximant phase (This is displayed in Table 1, situated in the UHV section of the project report). As a result of the change in constituents, surface studies in the UHV chamber can now be conducted. This is the reason for the selection of Ag-In-Gd quasicrystal and its approximant for the project.

1.3.1 Growth of Approximants

Approximants and *i-QC* have more flexibility in composition for the In-Ag-Yb system as compared with the Cd-Yb system (19). Like the compounds in the Cd-Yb system, the In-Ag-Yb *i-QC* melts in the same way and the approximants form by peritectic reactions i.e. the solid phase and liquid phase will together form a second solid phase at a particular temperature and composition. Since the *i-QC* is a congruent compound, a single grain of 10 mm in diameter is easily grown by using the Bridgman method. (7 p. Chap 4 pg 96)

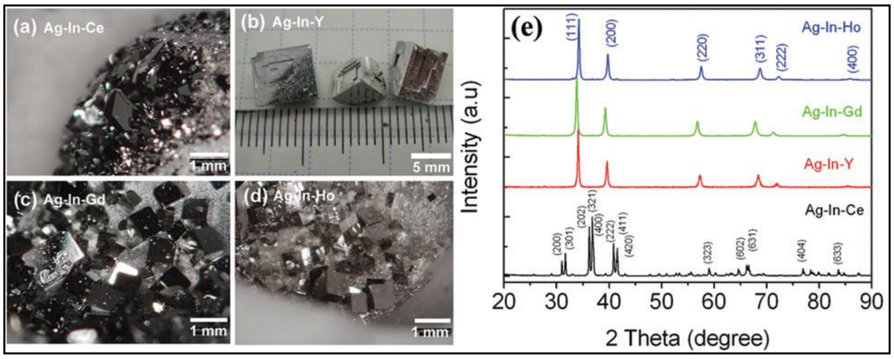

Figure 6: Macrograph of samples synthesized by the self-flux method in different systems: Ag–In–Ce (a), Ag–In–Y (b), Ag–In–Gd (c), Ag–In–Ho (d), as well as the related powder XRD patterns (e). Macrograph and the related powder XRD pattern of the Ag-In-Gd samples. (19)

The starting compositions were in the range of 30–45% Ag, 45–60% In and 6–10% RE, at a temperature in the range of 480–610°C. (19 p. Page 7). The atomic size of *RE* elements seems to be important in whether the formation of a quasicrystal or its approximant takes place.

1.3.2 Cd-Yb and Ag-In-RE Related Icosahedral Clusters

Icosahedral quasicrystals *(i-QCs)* can be classified into three classes according to hierarchic structures of icosahedral clusters derived from their corresponding approximants; the A1-Mn-Si, class, the Mg-A1-Zn, class and the Cd-Yb class (7). The structures of the atomic shells for the three classes are shown in Figure 7.

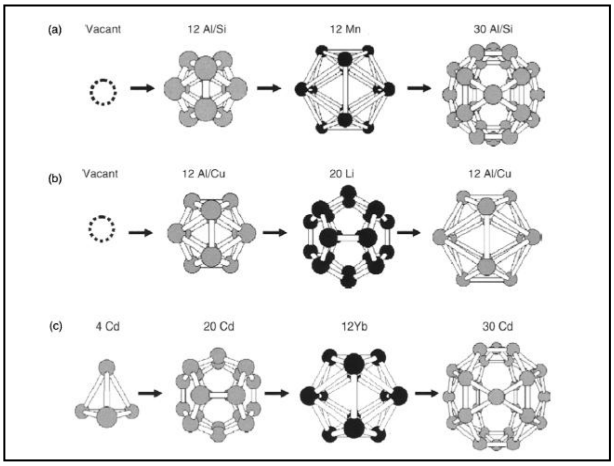

Figure 7: Clusters in icosahedral quasicrystals and their approximants :(a) The A1-Mn-Si class or Mackay icosahedral cluster: the centre is a vacant, 1st shell is an Al/Si icosahedron, 2nd shell is Mn icosahedrons, and the 3rd shell is an Al/Si icosidodecahedron. (7) (10)

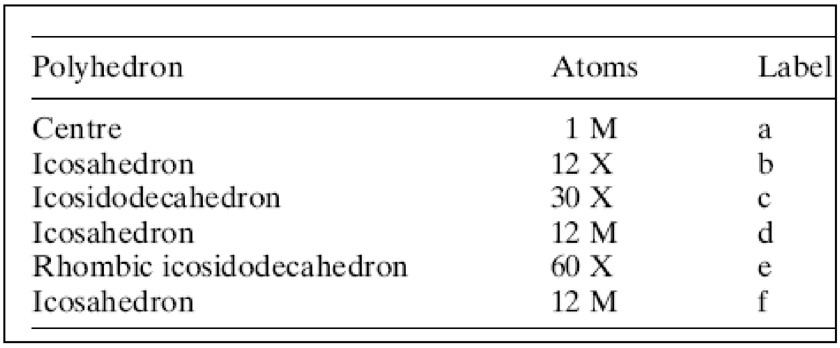

Polyhedron	Atoms	Label
Centre	1 M	a
Icosahedron	12 X	b
Icosidodecahedron	30 X	c
Icosahedron	12 M	d
Rhombic icosidodecahedron	60 X	e
Icosahedron	12 M	f

Figure 8: Polyhedra shapes found in icosahedral QC (20)

The shapes used to construct these clusters are shown in Figure & Figure 9.

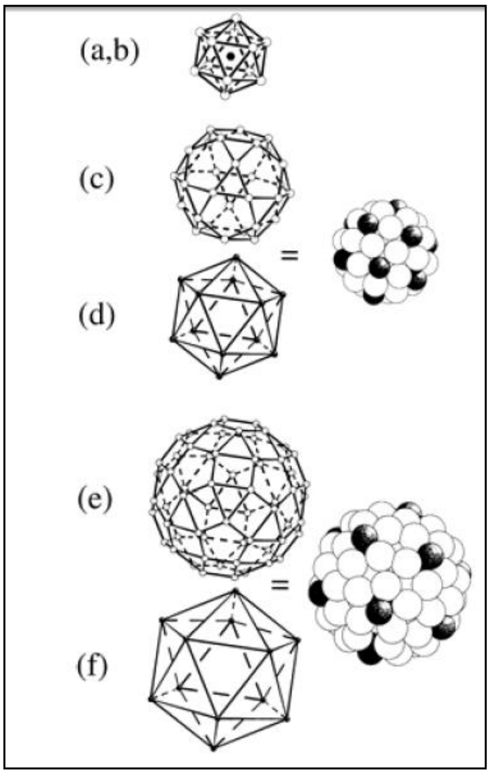

Figure 9: Various combination of icosahedral structures to form clusters. (20)

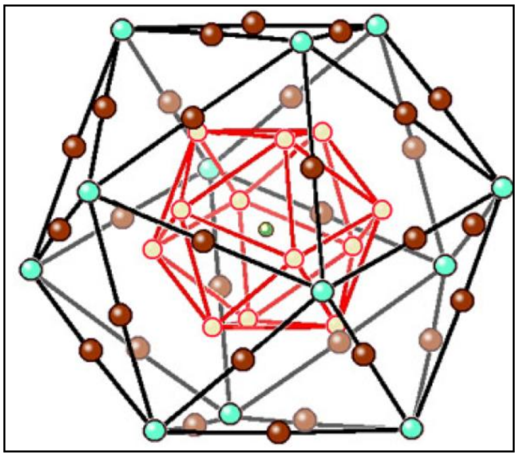

Figure 10: Mackay Type Cluster

First Shell: Icosahedral (12 vertices)

Second Shell: Icosidodecohedral (30 vertices)

Third Shell: Icosahedral (12 vertices)

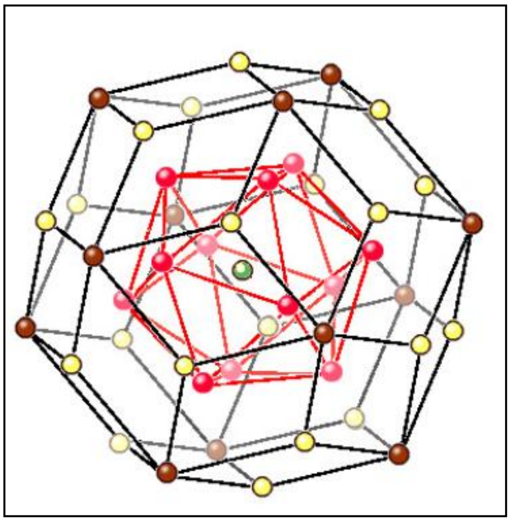

Figure 11: Bergman type cluster (20)

First Shell: Icosahedral (12 vertices)

Second Shell: Dodecahedral (20 vertices)

Third Shell: Icosahedral (12 vertices)

The third class of Cd-Yb is related to the Cd6Yb approximant, which has a bcc packing of identical icosahedral clusters. In the core of each cluster there is a tetrahedron created by four positionally disordered Cd atoms, which breaks the icosahedral symmetry (10). Icosahedral quasicrystals and approximants of the Cd-Yb class have been found in a large number of alloys which constitutes the largest one of the three classes *of i-QCs.* In the 1/1 approximant of the Ag-In-RE alloys, tetrahedra at the centre of the icosahedral clusters were also commonly observed. These are now referred to as Tsai type clusters. The analysis of the model in the latter sections of the report will draw comparisons with this form of cluster.

1.4 Applications of Quasicrystalline Materials

The most well known and first application of quasicrystalline materials, cam in the form of coatings for other metallic instruments for example the non-stick frying pan. The low co-efficient of friction found in quasicrystals is just one of the many exotic properties that have potential applications. Quasicrystals are also used as re-enforcing particles in alloys and steel, due to their extremely hard and brittle mechanical properties. Research into potential applications is ongoing, such as their use in hydrogen storage for hydrogen fuel cells. More applications are expected to arise from the continuing effort to describe the physical properties and structures seen in quasicrystals, highlighting the need for continued research in the field. (11)

2 Experimental Procedure and Techniques

2.1 Low Energy Electron Diffraction (LEED)

A crystal structure may be regarded as having two parts, a lattice and a basis. The lattice is a three dimensional array of points while the basis is the arrangement of atomic positions around each lattice point. The unit cell for a particular structure is usually the simplest possible unit of the structure which contains everything which is unique about the structure (21).

The plane of atoms defined in a crystal is defined by three co-ordinates and are labeled as the *Miller indices (h,k,l)* (22). These are the reciprocals of the fractional intercepts of the plane with axis **a,b**, and **c,** expressed in the form of the smallest whole numbers. Wherever an intercept is infinite, the corresponding index is zero. From this there is a reciprocal relationship to the wavevector **k** of a beam which is defined as:

$$\boldsymbol{k} = \frac{\boldsymbol{2\pi}}{\boldsymbol{\lambda}}$$

It is a measure of the momentum of the incident and diffracted beams. This inverse relationship between the wavelength and the wavevector comes from the de Broglie equation:

$$\lambda = \frac{h}{p}\ \text{, hence}\ \boldsymbol{k} = \frac{\boldsymbol{p}}{\hbar}$$

The change in wave vector of a beam scattering from a plane of atoms will determine the direction of any emergent refracted beams i.e. the diffraction pattern obtained is a reflection of the changes in wave vector. It is possible to create a reciprocal lattice, where the distances between each point are inversely proportional to distances within the real lattice (22).

A diffracted beam of electrons can be detected from a crystal whenever constructive interference takes place between two planes of atoms. By applying the laws of conservation of momentum, the Ewald Sphere construction can be applied (22) to calculate distance between lattice points in real space.

2.2 Electron Diffraction

Electrons as charged particles interact very strongly with matter. The mean free path of low energy electrons (<500eV) is of the order of a few tens of Å. The wavelength of such an electron is also of the order of an Å, comparable to interatomic spacing and thus suitable for diffraction experiments. A monochromatic beam of electrons can also be produced, essential for surface study. As the electrons are low energy it is appropriate assume that the diffraction pattern produced is from the topmost layers of the surface, giving us a 2-d surface unit measurement (22).

2.3 LEED Apparatus

The elastic backscattering of low energy electrons incident normally on a crystal surface forms the basis of the technique of low energy electron diffraction. LEED requires the use of Ultra High Vacuum technology. A schematic of the LEED apparatus is shown in

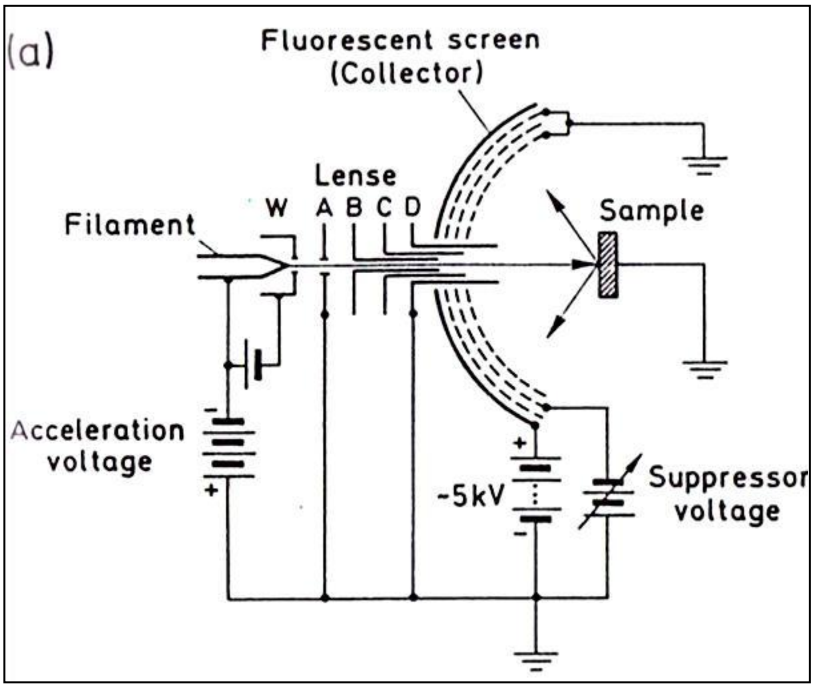

Figure 12: Schematic of LEED apparatus (21)

An electron beam of variable energy is produced by an electron gun and is incident on the sample. The electrons are backscattered from the surface onto a system of grids surrounding the electron gun. Backscattered electrons are either elastically scattered, creating the LEED pattern, or inelastically scattered (99% of total Flux). The latter are not required and are removed using a negatively bias voltage filter, as they otherwise contribute to a bright, diffuse background across the whole of the LEED screen. An accelerator voltage is also used, of positive potential (approx 5KV), to give elastically scattered electrons enough energy to cause an excitation on the fluorescent screen and produce the bright LEED spots. The potential across these grids is adjusted to minimise the diffuse background to the LEED pattern. The pattern may be recoded using a mounted camera viewing the LEED screen (21).

2.4 LEED Analysis

LEED is extremely sensitive to surface contamination and roughness, so the appearance of bright sharp spots is a good indicator of how clean and ordered a surface is, useful to know for further experiments (22). The LEED pattern can be used to obtain information about the surface symmetry, surface reconstruction or imperfections in the surface, such as steps, multiple grains or islands. It can also be used to determine if any molecules on the surface are absorbed in an ordered or random way. As the energy of the electrons is increased, the bright spots move towards the centre of the screen. Usually, the incident electron beam is normal to the surface, in which case a symmetrical LEED pattern is obtained, converging towards the specular beam.

The energy of the electron beam is given by:

$$E = \left(\hbar^2/_{2m}\right)k^2 \text{, where} \quad \boldsymbol{k} = {}^{2\pi}/_{\lambda}$$

Therefore the wavevector increases with an increase in the electron beam. There are also, as a result, more spots visible on the screen and spacing between spots decreases (22).

2.5 Scanning Tunneling Microscopy (STM)

Scanning tunneling microscopy' (STM) is a powerful tool for the determination of the structural and electronic properties of surfaces. A sharp metal tip is brought close enough to the sample surface that electrons can tunnel quantum mechanically through the vacuum barrier separating tip and sample. This tunneling current is extremely sensitive to the gap (the height of the tip above the surface). In vacuum tunneling, the potential in the vacuum region acts as a barrier to electrons between the two metal electrodes, in this case the surface and the tip. (23)

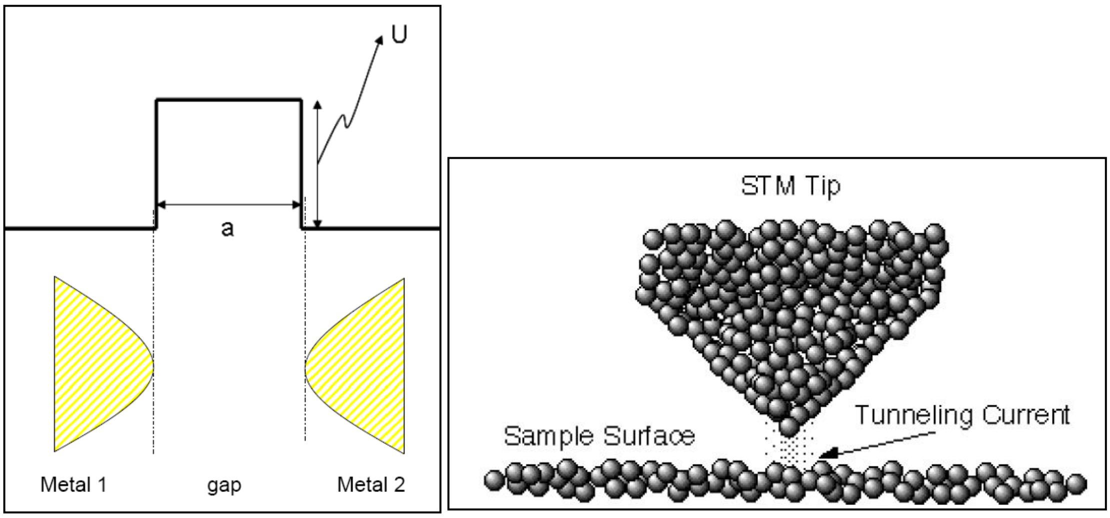

Figure 13: Potential barrier and tunneling between tip and surface (24)

The transmission probability, or the tunneling current, thus decays exponentially with barrier width ***d*** as:

$$I \propto e^{-2Kd}$$

Equation 3: Exponential dependency of current flow on tip sample separation (25)

For tunneling between two metals with a voltage difference *V* across the gap, only the states within *V* above or below the Fermi level can contribute to tunneling, with electrons in states within *V* below the Fermi level on the negative side tunneling into empty states within *V* above the Fermi level on the positive side. As most work functions are around 4-5eV, or 2K ~2Å^{-1} the tunneling current drops by nearly an order of magnitude for every 1 Å of vacuum between the conducting sample and tip. Therefore tunneling can only be observed at very small distances. To make use of this, control of the tip across very small distances is necessary.

2.5.1 Tip Control

The position of the tip in three dimensions is accurately controlled by piezoelectric drivers. The tip is scanned in the two lateral dimensions, while a feedback circuit constantly adjusts the tip height, to keep the current constant. A constant current yields roughly a constant tip height, so the shape of the surface is reproduced by the path of the tip, which can be inferred directly from the voltage supplied to the piezoelectric drivers. It is also possible to use a slower feedback for the tip height, so that the height remains constant above the average surface, and small features are reflected in fluctuations of the current, rather than in the tip height.' However, this "constant height" mode of imaging ***is*** only practical in special cases where the surface is extremely flat, and is not fundamentally different from the usual "constant current" mode, so it is not discussed separately here (26).

2.5.2 Tip

The tip is a crucial component of the STM. The geometry and chemical identity of the tip influences both topographic and spectroscopic measurements. The best images are obtained when tunneling is limited to a single metallic atom at the end of the tip. Anomalous imaging artifacts will appear when simultaneous tunneling occurs through multiple atoms on the tip. When certain metal wires such as tungsten are fractured, or cut. The result is a rugged surface with a single atom as the endpoint. There is a strong dependence of the tunneling current on the tip-sample separation, and the STM will "find" the atom that is protruding toward the sample. Tungsten is most commonly used in UHV, where oxidation is not a factor. Tungsten has the advantages of being relatively inexpensive and easily etched to produce the desired macroscopic tip shapes (26).

2.5.3 Repair of STM Equipment

During the project, replacement of the wire connected to the sample plate, providing a bias voltage, was required. Images were taken to display the configuration of a functional system and to better understand the inner workings of an STM, as shown below:

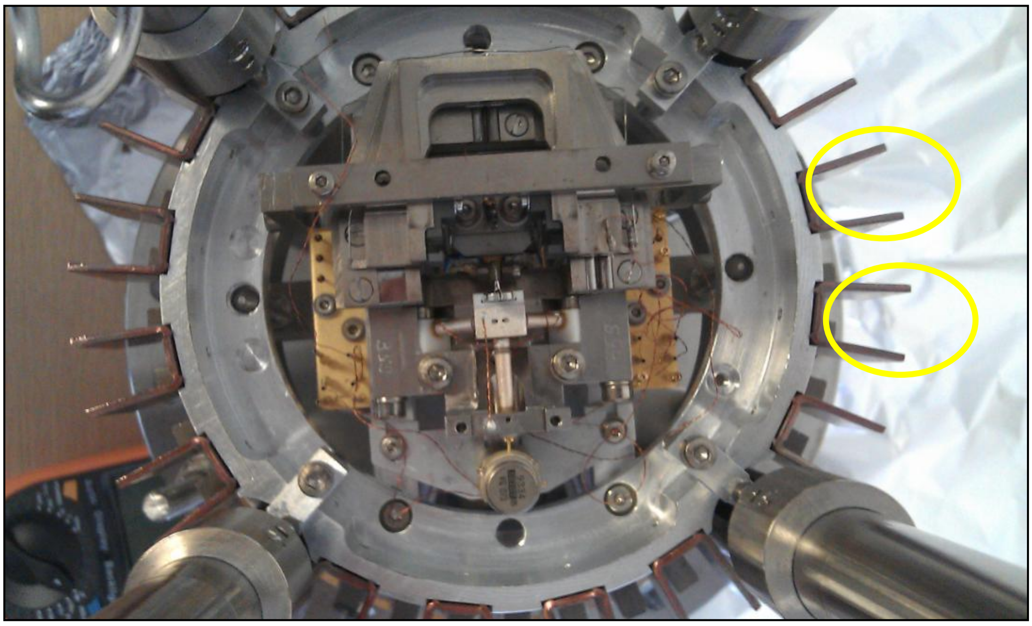

Figure 14: Magnetized system for tip stabilization (Rectangular shaped copper components)

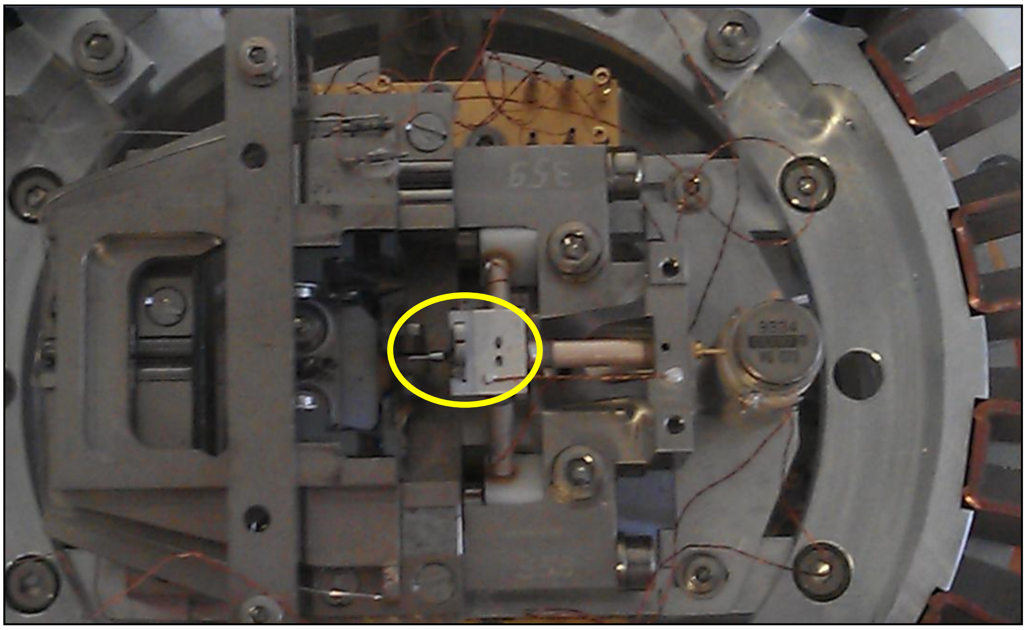

Figure 15: STM tip in a functional system

Highlighted in the Figure 14 & Figure 15, are the magnetized copper components, used to stabilize the STM during data acquisition and the STM tip that is scanned across the sample surface.

2.5.4 UHV chamber

An ultra high vacuum chamber is used to achieve pressures of around 1 x 10^{-9}mbar and lower. This is useful in surface science experiments in which the sample that is probed, must be free of contaminants, to obtain information about the structure of the surface. (18)At a pressure of 1 x 10^{-6} mbar, a single layer of contamination will form on the surface within one second, which makes resolving the surface structure of the sample impossible at this pressure. UHV chambers are typically constructed from stainless steel, as this material possesses a low out gassing rate, essential for maintaining the required pressure. (27) A series of valves and pumps are used to achieve pressures of up to 1 x 10^{-10} mbar. Typically a rotary pump, turbo molecular pump, ion pump and a titanium sublimation pump are used, which are discussed further on in the section.

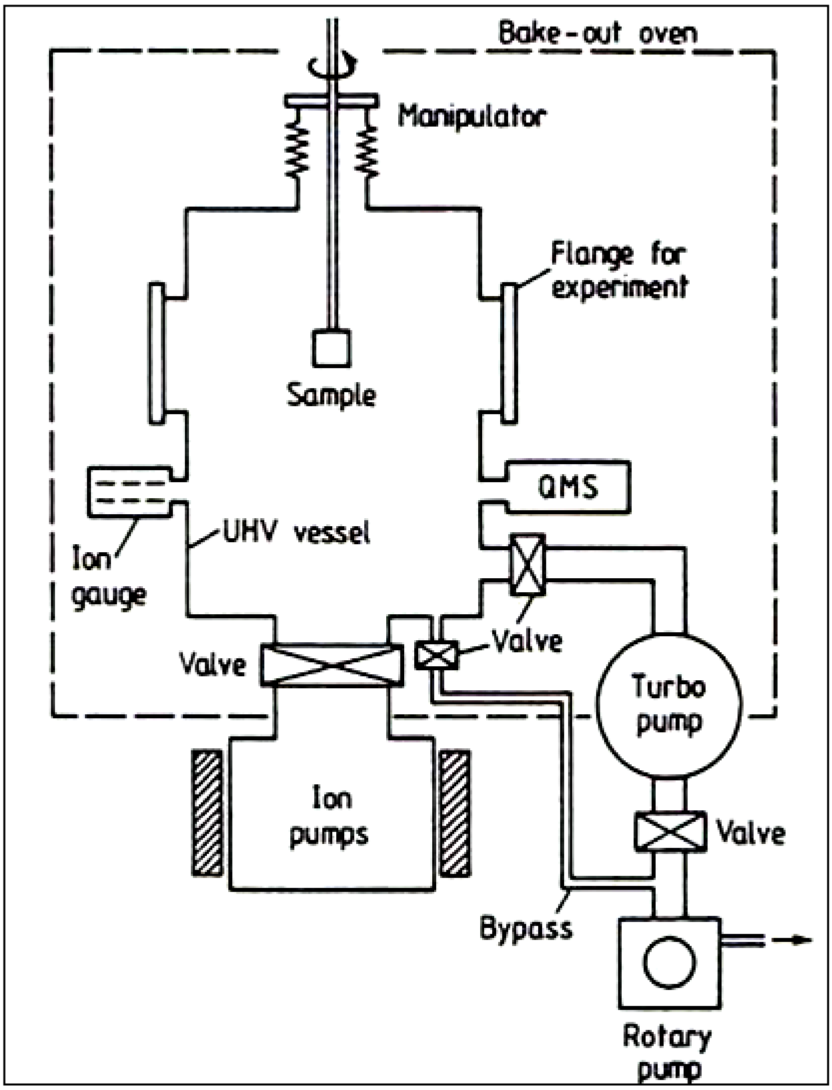

Figure 16: Schematic of UHV chamber (27)

Finally the system has multiple chambers, in which the sample can be positioned for studies with the variety of instruments incorporated (e.g. STM, LEED, XPS, UES) using a manipulator, which is controlled from the outside of the chamber by the user. Also, to achieve a low pressure a procedure known as “baking” is necessary. This process involves heating the entire system to a high temperature, in order to remove the thin film of water that may build up in a chamber and contaminate the sample. This is especially necessary when the chamber has been vented to the atmosphere. Only certain materials can be used for study in a UHV chamber. This is because the temperature at which a material will vaporize decreases with pressure (2). An example of this is shown in the table below:

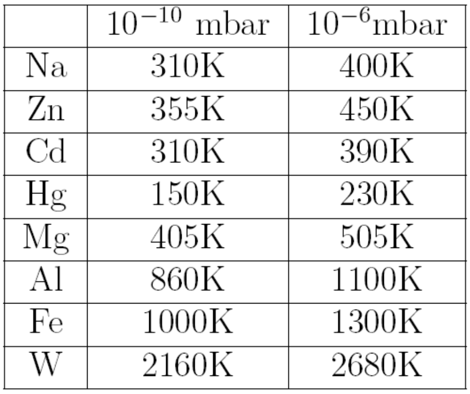

	10^{-10} mbar	10^{-6}mbar
Na	310K	400K
Zn	355K	450K
Cd	310K	390K
Hg	150K	230K
Mg	405K	505K
Al	860K	1100K
Fe	1000K	1300K
W	2160K	2680K

Figure 17: Vaporization temperature of various Materials depending on atmospheric pressure (2)

For example the table displays Cd has a low vaporization temperature at the required pressure for UHV surface analysis. Therefore it is unsuitable (28). This is the reason for the replacement of Cd-RE (RE= rare earth) systems, with similar alloys such as the one studied in this project, Ag-In-Gd. This alloy has a relatively high vaporization temperature at low pressure and consequently surface studies can be performed under UHV.

2.6 Experimental Procedure

The Ag-In-Gd approximant sample was grown using the self flux growth method by Tamura *et al*. The sample was of the dimensions 4 mm x 4 mm as shown in Figure 18 . (29)

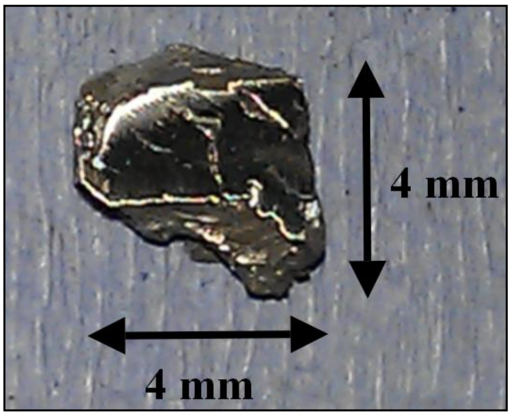

Figure 18: Dimensions of Ag-In-Gd approximant sample

Rubber gloves were used when handling the sample. The sample tweezers and metallic preparation dish were cleaned with ethanol during every break in the preparation cycle. Initially the sample surface was dull and hazy. The sample was polished until a mirror like surface was achieved, using a diamond paste of consecutively smaller grain, 6 µm, 1 µm and 0.25 µm. The 6 µm paste was spread evenly onto 42 µm sandpaper, which was adhesively fixed to the preparation dish. The sample was polished in a figure of eight motion (29). After this cycle, the sample was then placed in an ultrasonic bath to remove particles from the surface. The process was repeated using the 1 µm and 0.25 µm paste with a 20 µm sandpaper. The sample was then mounted to the plate for insertion into the chamber. Initially an attempt was made using a silver based adhesive, however it was discovered in the annealing process that this made the sample surface look particularly hazy. In light of this, the preparation process was repeated and the sample was instead mounted, using wire, to the plate. The sample was then introduced to the UHV chamber, where a pressure no greater than 4×10^{-9} mbar was achieved using rotary pump to achieve a pressure of 1×10^{-3}mbar, turbo molecular pump to obtain a pressure of 1×10^{-6}mbar and an ion pump to obtain a pressure as low as 1×10^{-10}mbar. In addition to this a titanium sublimation pump can be used to regularly reduce the pressure during an experiment. Once positioned in the chamber, the sample underwent several cycles of sputtering and annealing. During the surface of the sample is bombarded with energetic argon ions to remove the top layer of the surface along with contaminants and oxide layers (29). After sputtering the chemical balance of the surface will be altered and deformed as the lightest constituents may be depleted, leaving the surface composition different to the bulk (30). To regain the chemical composition of the surface via bulk diffusion, it was annealed to a temperature of 450^{o} C for a 4 hour period. This sputtering and annealing process also has the effect of producing steps and terraces on the surface of the sample, which were the target of the investigation (31). Initially the annealing time for this sample was 1-2 hours with 30 minutes of sputtering, through approximately 10 cycles. From this preparation, a LEED pattern was obtained. From the room temperature STM as shown in Figure 19

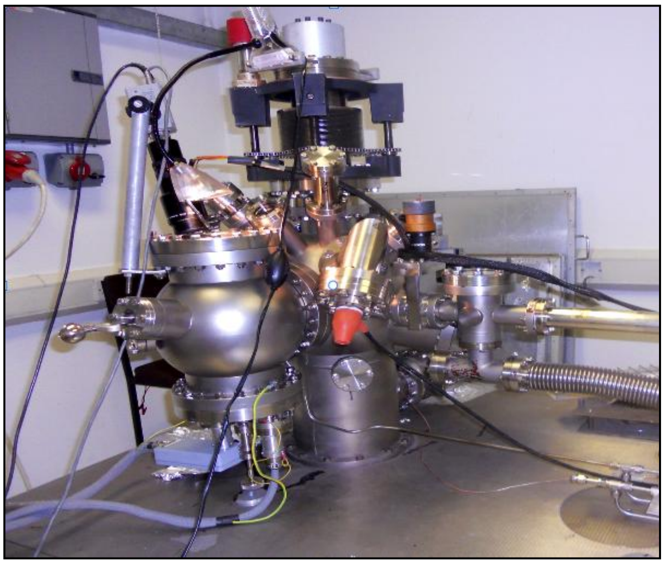

Figure 19: Room Temperature UHV chamber in the Surface Science Research Centre, the University of Liverpool

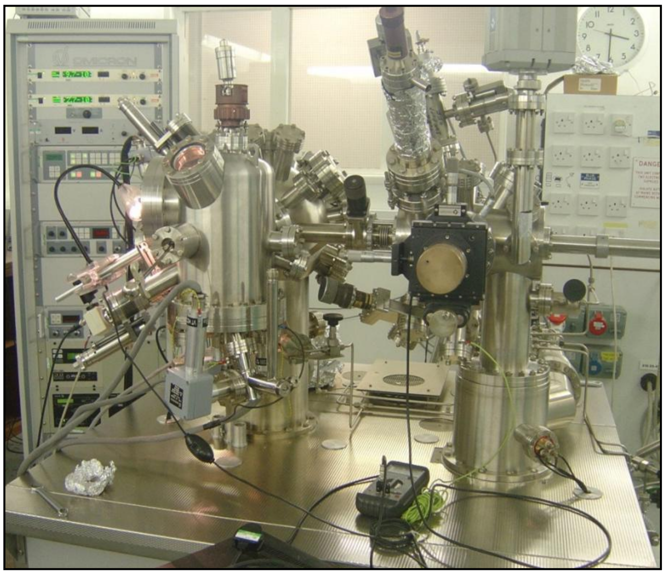

Figure 20: Variable Temperature UHV chamber in the Surface Science Research Centre, the University of Liverpool

However, the STM data was only acquired when the sample was extracted, re-polished, transferred to the variable temperature chamber and prepared over 5 subsequent cycles consisting of 4 hours annealing followed by 30-45 minutes of sputtering. The LEED data was acquired over an energy range of 27eV to 41eV. This produced a recognizable diffraction pattern from the sample. The STM data was taken at a bias of 1-2.5V, with frequent pulsing of the tip required to regain image resolution. This may have been required due to previous tip damage, whilst acquiring data from the sample Atomic resolution using STM was not achieved with a maximum resolution of 20 nm x 20 nm.

2.7 Experimental Summary: Preparation Parameters and Improvements

By successfully preparing the sample, the preparation parameters were optimized for the acquisition of STM and LEED data and the first aim of the project was accomplished. Parameters for preparation of 1/1 quasicrystal approximant of Ag-In-Gd consist of:

- Polishing using 6 µm, 1 µm and 0.25 µm diamond paste.
- Sputter and Anneal for 4 hours and 30-45 minutes respectively for 10-15 cycles

However, there is room for refinement of these parameters, as they may be affected by the particularly small size of the sample. It would be useful in the future to obtain a larger sample, in the first instance to allow easier preparation and secondly to see how the sample size may affect the preparation time scales needed. Also, the LEED pattern although useful, could have been improved, requiring further testing of procedures to gain optimum diffraction condition

3 Bulk Structure Model of Ag-In-Gd Approximant

The theoretical model for the bulk structure Ag-In-Yb 1/1 approximant, provided by Shimoda *et al* (32), was used at length, to help understand the data taken from the Ag-In-Gd 1/1 approximant sample. In the model the atomic positions held by Yb were replaced with Gd .The model is spherical and of radius 50Å. It is known that surfaces form from the highly dense atomic planes in a material (22) (18). Therefore the model was manipulated in the modeling software Igor, to look only at the miller planes that contained a high density of atoms. This data was then exported to Microsoft excel, where it was put into a readable form for the Imaging software JMol. This then allowed the construction of an xyz image, in which the different planes could be rotated and examined. After studying the model, it was possible to understand the predicted atomic positioning of the constituent atoms in the different Miller indices. Identifying the theoretical structure, spacing and symmetry of the unit cell was important for comparison to the LEED and STM data that was collected.

3.1 Analysis of the Ag-In-Gd Approximant Bulk Model

As the surface of the Ag-In-Gd sample was grown in the (100) Miller direction, the model was manipulated to display the high atomic densities in this plane. As the structure is Icosahedral, the theoretical bulk structures in other Miller planes were also examined to use in comparison with any other possible directions detected on the surface of the sample. The model of the (100), (010) and (001) planes were first studied, followed by the (310) due to imaging of facets in multiple planes. In each case the structure, spacing and symmetries were examined in the relevant high density planes. The following colour coding will be used to identify Ag/In/Gd atomic positions, along with sites of shared occupancy.

C.Center	⬜
Yb	🟩
In1	🟩
In1/Ag1	🟦
In2/Ag2	🟦
In3/Ag3	🟦
In4/Ag4	🟪
Ag5	🟪
In6/Ag6	🟪

Figure 21: Colour coding of Bulk Model for Ag-In-Gd 1/1 Approximant (32)

3.1.1

3.1.2 (100), (010) and (001) Miller Planes

Below is the spherical model, first in the XZ plane and then in the XY plane, cut in the (100) direction.

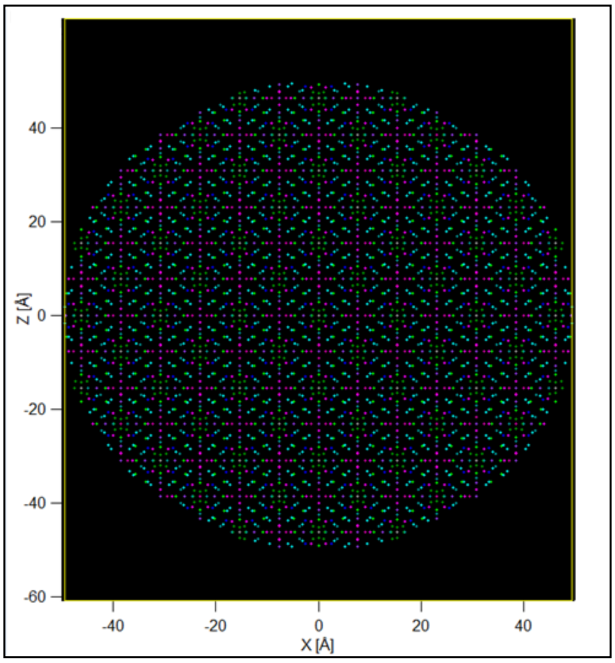

Figure 22: Spherical Bulk model, positioned in the (100) XZ plane (32)

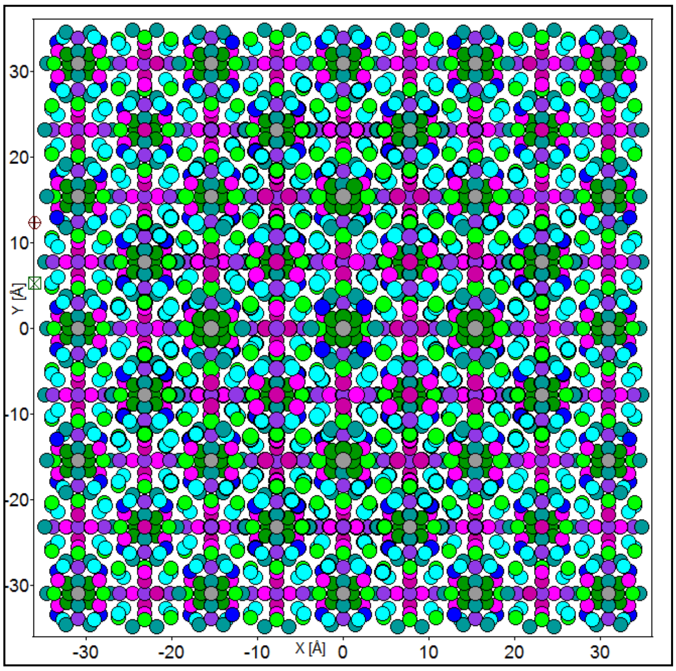

Figure 23: Spherical Bulk model, positioned in the (100) XY plane (32)

From this, it seems the atoms form in clusters around cluster centres, throughout the model. The high density planes throughout the model in the (100) plane can be seen from Figure 24.

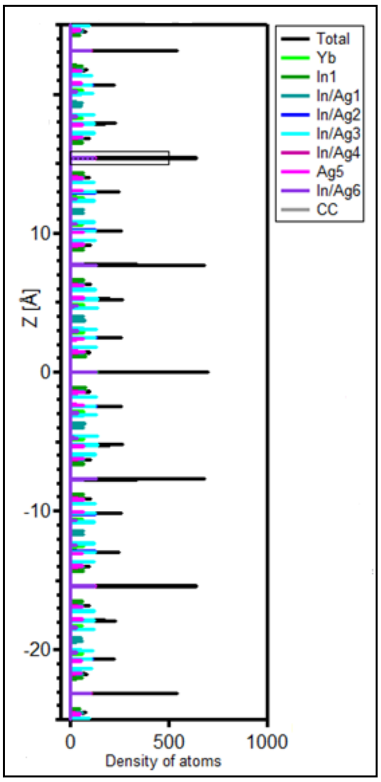

Figure 24: High density planes in the (100) Miller plane (32)

We can see the highest density planes are spaced by 7.7Å. The three high density planes investigated are highlighted accordingly. The XY plane of the highest density is displayed in Figure 25.

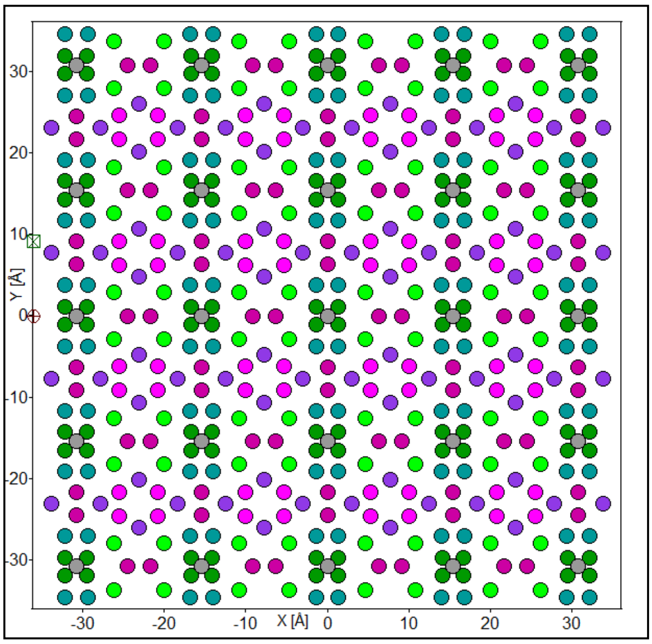

Figure 25: Bulk model, High density plane in the (100) Miller direction. (32)

We can see that the atoms in this high density plane again form clusters. These clusters centres are arranged over a square lattice which, would suggest that the structure is simple cubic. However if the model is extended over two high density planes in the Z direction, two interlocking square lattices are observed.

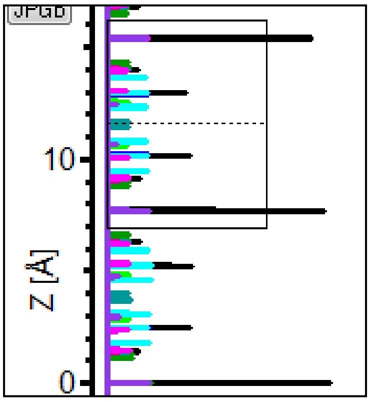

Figure 27: 0.77nm spacing between high density planes in (100) (32)

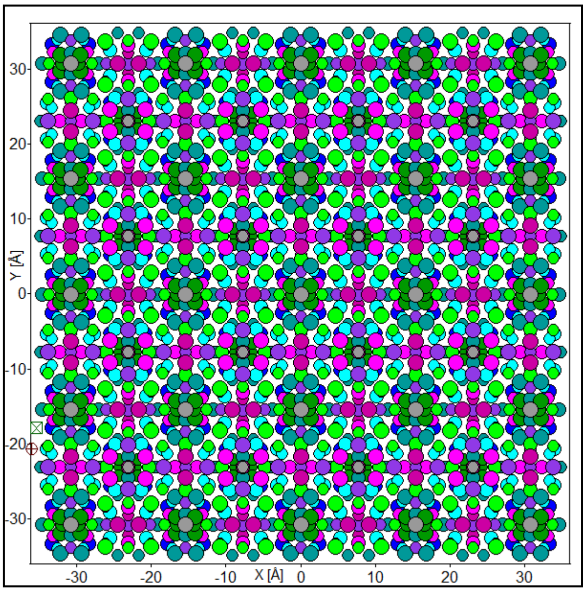

Figure 26: XY plane of Bulk model extended over an entire unit cell in the (100) Miller plane. (32)

By growing the model in 3D , the Ag-In-Gd 1/1 approximant shows BCC cubic structure (Two interlocking simple cubic lattices).

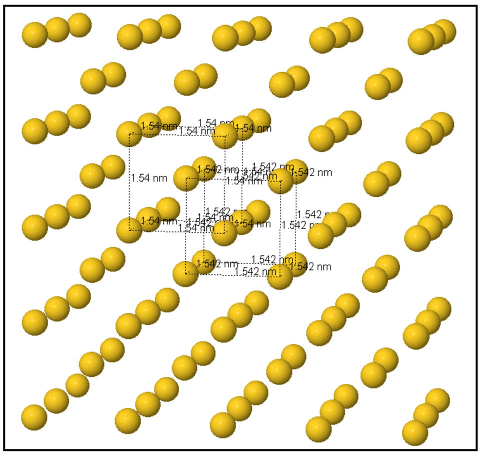

Figure 28: 3D representation of Bulk model displaying BCC structure of cluster centres in the (100) plane.

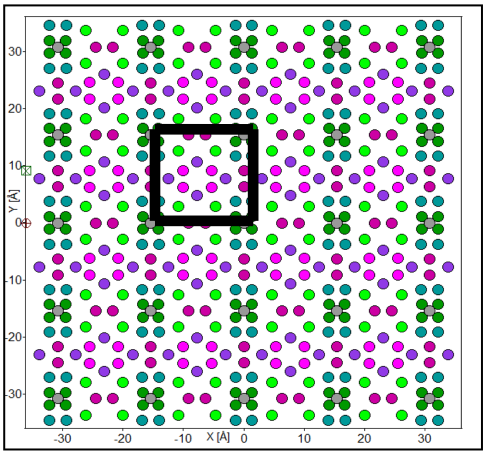

Figure 29: Cubic unit cell displayed in (100) plane, spacing 1.54 nm (32).

The model shows the cubic unit cell in the (100) plane has a spacing of 1.54nm. The clusters seen in the model are spread across a BCC lattice with this spacing between cluster centres. The model for the other high density planes is displayed below.

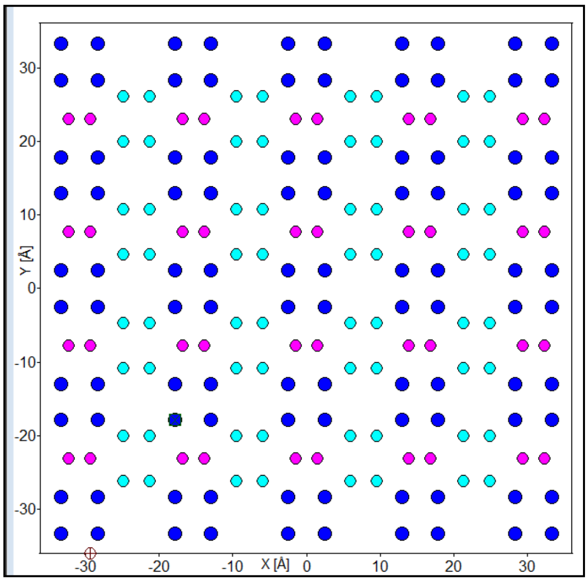

Figure 30: Inverted high density plane in (010) (32).

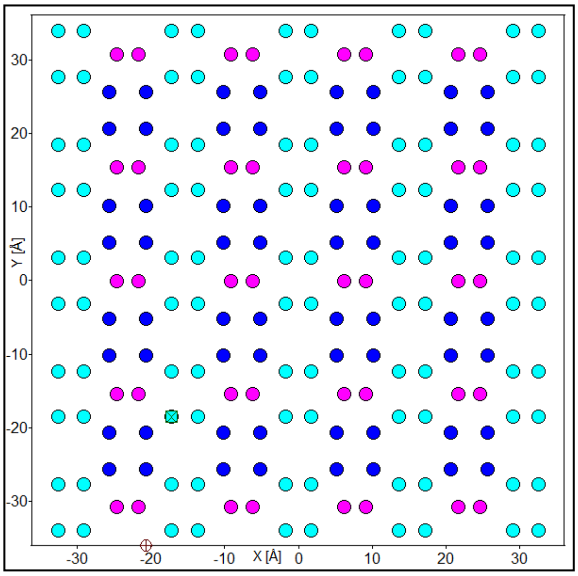

Figure 31: Inverted high density plane in (001) (32).

We find the same unit cell spacing of 1.54nm and structure as in the previous Z plane. Individually each plane repeats throughout the structure every 0.77nm. These two planes are inverted, with a separation of 0.28nm. They are located from the high density atomic plane diagram at positions of 10 Å and 13 Å respectively. To determine which is preferred for surface formation analysis of experimental results is required. To investigate the constituents of the clusters, the model was adapted to display a 3D representation of a single cluster.

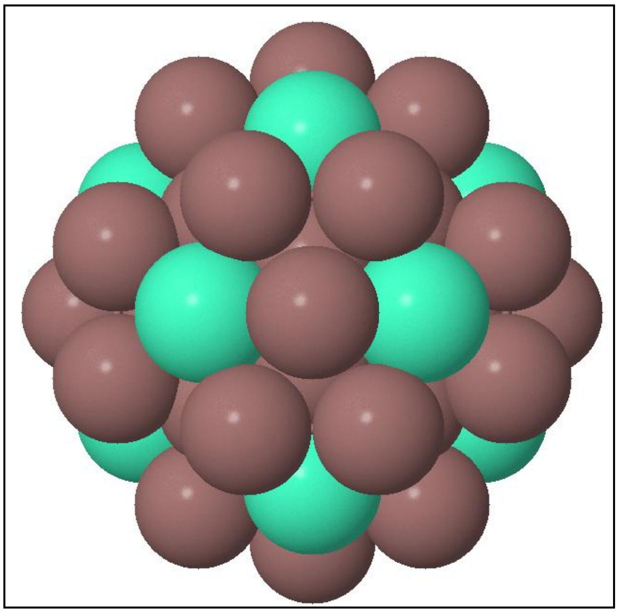

Figure 32: 3D model of (100) orientated of atomic clusters.

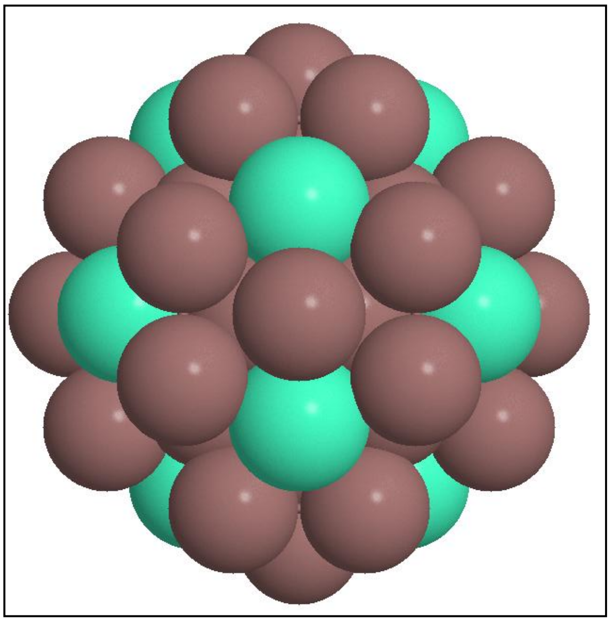

Figure 33: (010) and (001) orientation of atomic clusters

The 3D model of the clusters above confirms that they are icosahedral in shape. Therefore, even though the lattice is BCC structure, the (100), (010) and (001) directions look different. The 010 and 001 planes are shown below in the XZ and XY orientations (i.e. at 90^{o} to the (100) plane).

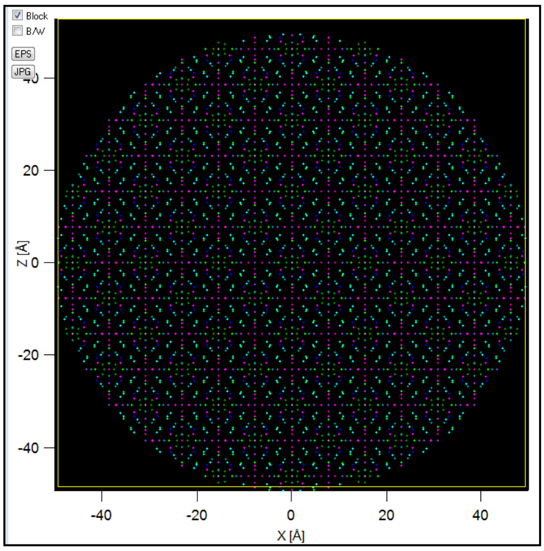

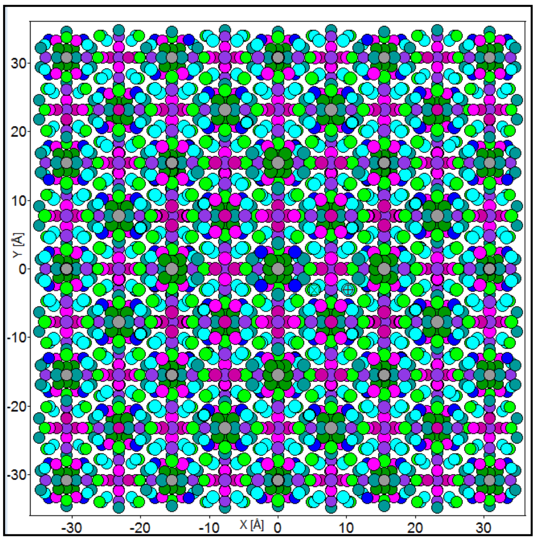

Figure 34:(010) and (001) model orientation in the XY plane (left) & Figure 35: (010) and (001) model orientation in the XZ plane (right) (32).

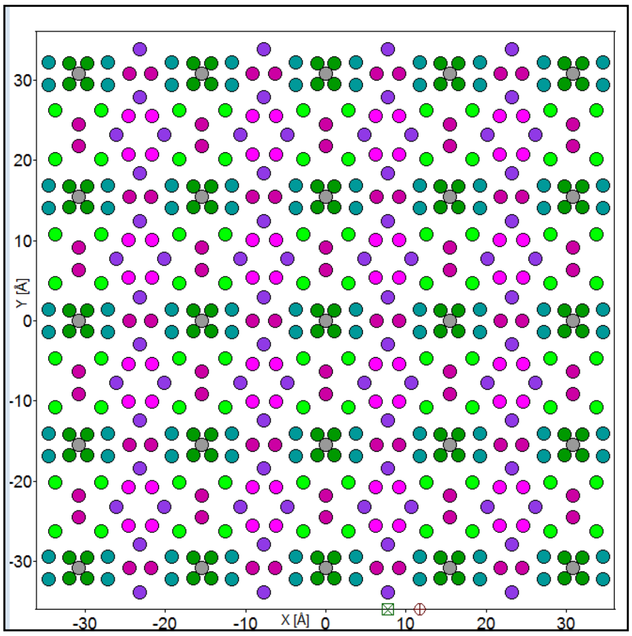

Figure 36::(010) and (001) model orientation in the high density XY plane (32)

As predicted, the (010) and (001) high density planes are identical to the (100) but rotated by ±90°, providing asymmetry in these directions.

3.1.3 (310) Miller Plane

The XZ plane of the model in the (310) plane is shown below at an angle of 18.44° to the (100) plane.

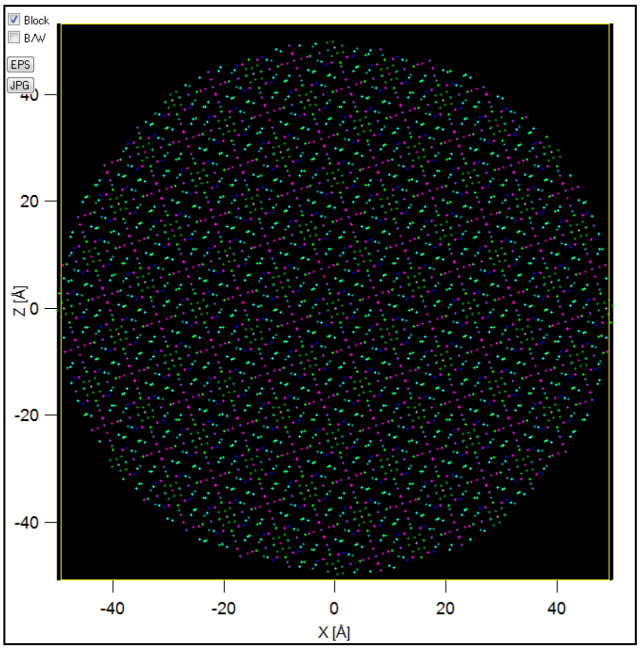

Figure 37: Bulk model of Ag-In-Gd in the (310) Miller XZ Plane

There is no explicit high density Z plane in the (310) direction of model, however at an angle of 1-3° either side of 18.44° for the (310), the atomic densities are noticebly larger.

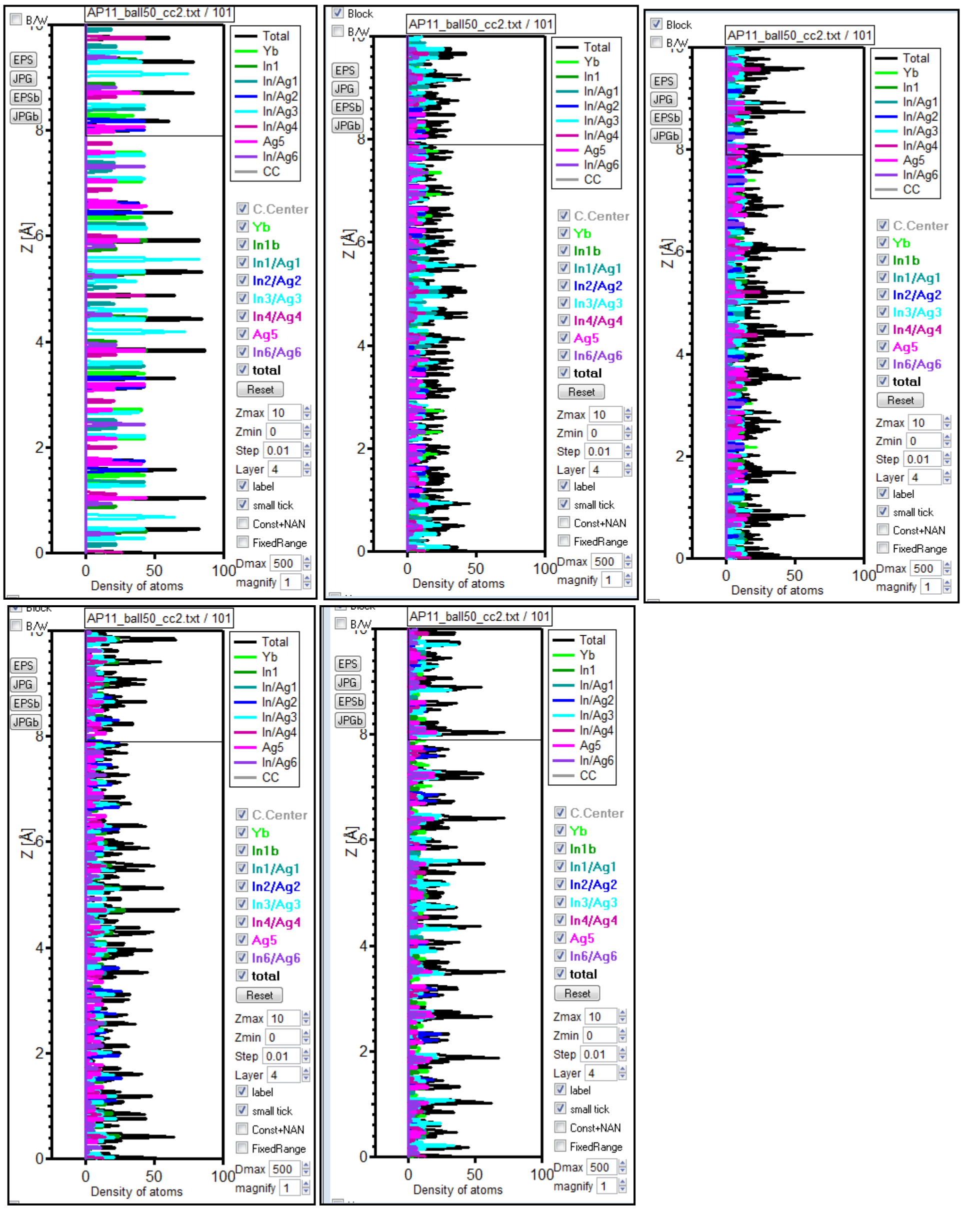

Zmax 10
Zmin 0
Step 0.01
Layer 4
☑ label
☑ small tick
☐ Const+NAN
☐ FixedRange
Dmax 500
magnify 1

Figure 38: High density atomic planes at an angle of 18.44° 17.44 °,16.44 °,19.44 ° and 20.44 ° respectively with the (100) plane. (32)

The (310) has higher density planes than those at neighbouring angles; however they are closely packed and appear to be approximately the same density. Consequently, formation in this plane would result in small terraces with many different step heights, which is not particularly favourable. Still, the (310) plane is imaged upon the surface of the sample, but without these terraces of different step heights as will be discussed later. This is an interesting contrast with the model and may be explained by possible cluster preservation at the surface.

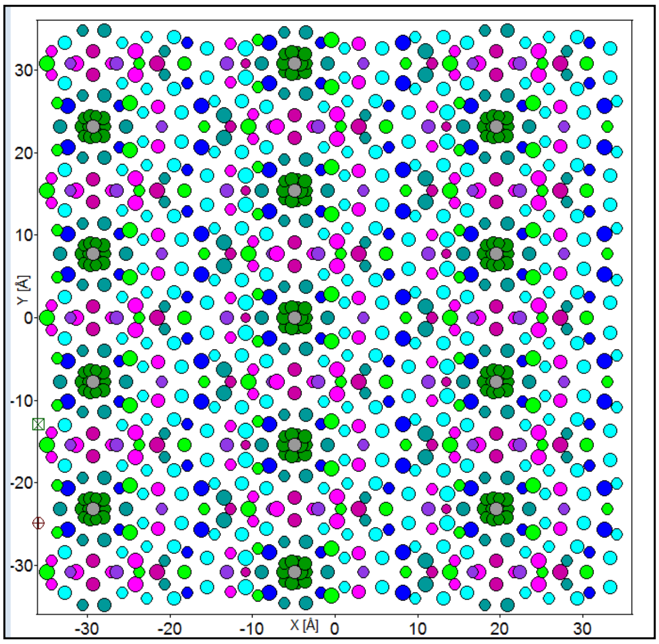

Figure 39: Unit cell structure and spacing in the (310) model plane (32)

In the bulk model (310) plane, the unit cell is spaced across two clusters and is rectangular in shape. This is expected from the (310) plane in a BCC lattice. This is confirmed when by the (310) model in 3D as shown below.

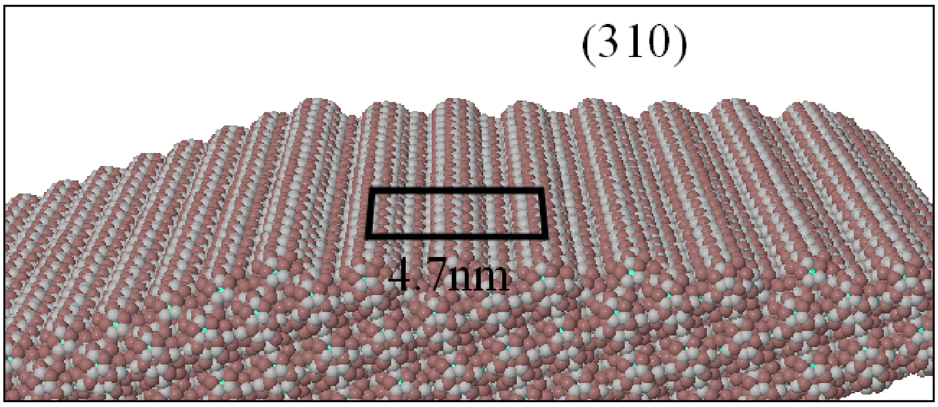

Figure 40: 3D representation of (310) surface with clusters preserved.

This model has been adapted to preserve the clusters on the sample surface and compare with the STM data acquired from the sample. In summary, the model provided by Shimoda *et al*, has been extremely useful in understanding the data acquired. These comparisons will now be discussed and any inconsistencies highlighted.

4 Results and Analysis

4.1 STM Analysis

Scanning tunneling microscopy was performed on the Ag-In-Gd surface. Atomic resolution was not achieved, yet a significant amount of surface structuring was observed, due to the apparent preservation of large scale atomic clusters on the surface. Analysis was performed to investigate the possibility of cluster preservation and draw comparisons between the data and the theoretical model.

4.1.1 Analysis Techniques and Software

The data gathered using STM was analysed using the "Gwyddion" STM software along with "WSxM" (33)to measure atomic spacing and identify symmetries. This software was also used to generate 3D images from the data and generate fast Fourier transforms, providing information on the surface periodicity. The modelling software "Igor" was used to view and manipulate the Ag-In-Gd model and select the correct surface planes for comparison with data. The model was further adapted to construct a 3D representation of the surface, using Microsoft Excel and the image rendering software "JMol". The STM data was also converted to the correct format for input into "JMol", producing a more beneficial 3D display. "Vesta" was used along with Microsoft excel, to generate a model that preserved the clusters on the sample surface. "Adobe Photoshop CS.5" was used for image enhancement of the LEED data and analysis, providing length measurements when properly configured.

4.1.2 Multiple Terracing and Surface Facets

At 1.2µm x 1.2µm resolution and bias voltage of 2.5V, the “streaking” pattern was observed as shown in Figure 41. After magnifying this region, multiple facets in the surface were detected.

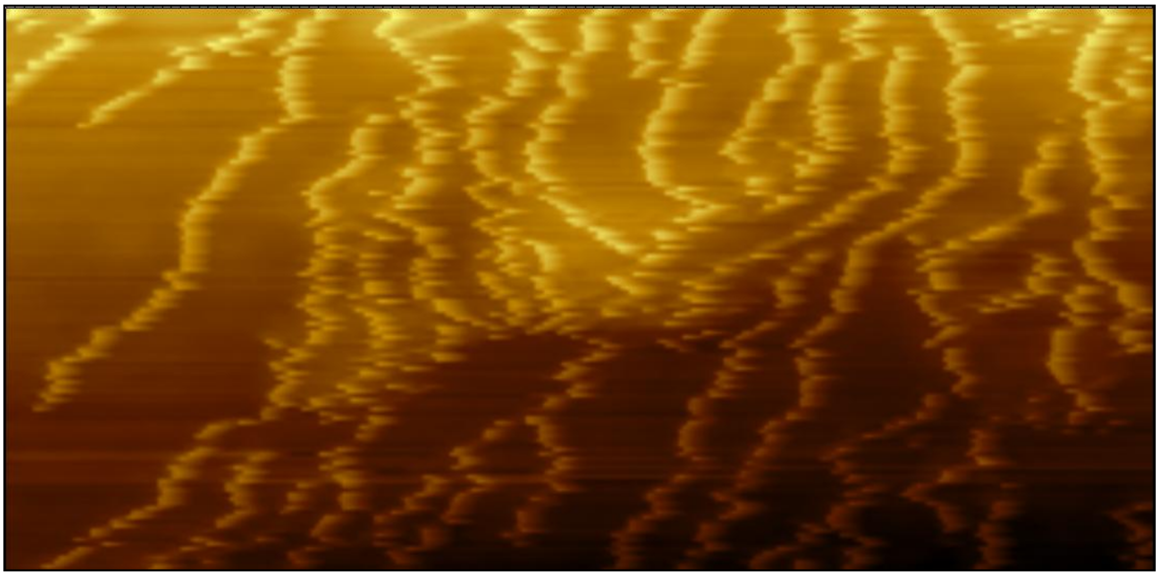

Figure 41: STM data, 1 .8 µm x 1.0 µm resolution at bias voltage of 2.5V, displaying multiple surface facets.

At a resolution of 200nm x 200nm facets in the surface were observed, producing terraces in the expected (100) plane, accompanied by terraces orientated in an unidentified plane. Faceting is shown by the raw data in Figure 42 and in a 3D representation of the data in Figure 42.

Figure 42: STM data 200nmx200nm showing surface facets in multiple planes, ***Figure 43: 3D representation of***

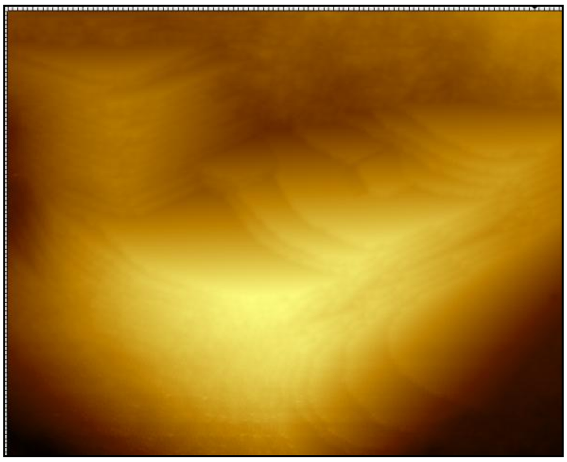

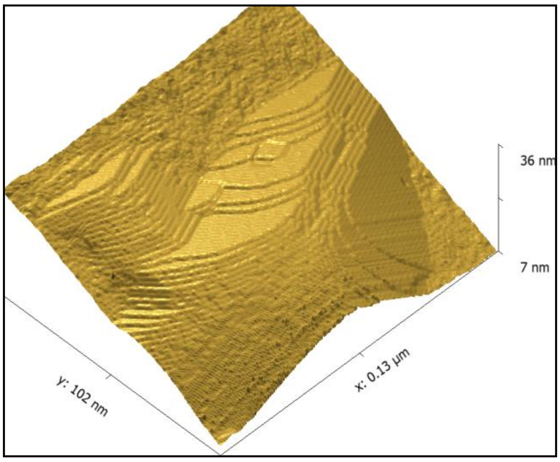

surface terracing and multiple facets

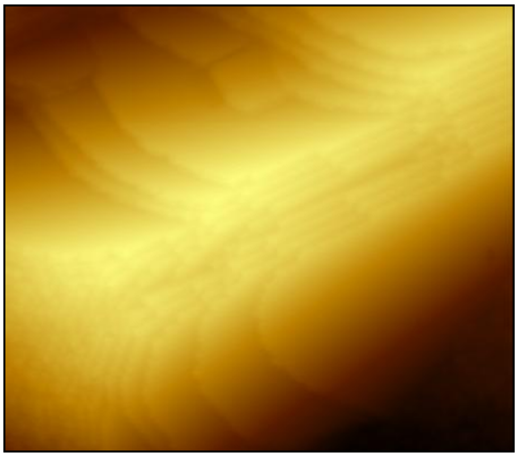

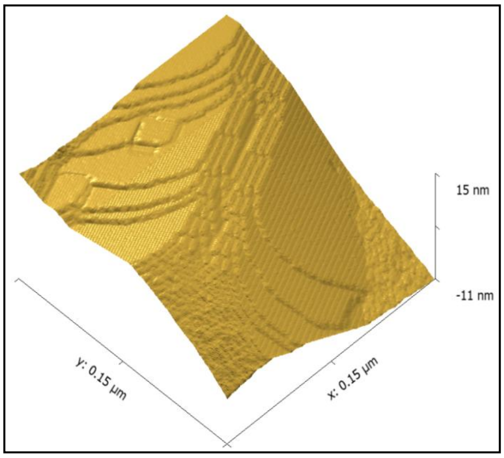

Figure 44: STM image of surface facet, 153nm x 153nm resolution (Left). ***STM image of surface facet, 153nm x 153nm resolution, Figure 45: 3D representation of surface facet (Right).***

This interesting region of the surface was magnified in order to confirm the facet contained terraces in (100) and obtain data with a high enough resolution to identify the direction of the unknown plane. Figure 44 shows the facet magnified to 153nm x 153nm. There is another terrace direction at the apex of the (100) and (310) facet as shown in

Figure ***46***. Although the Ag-In-Gd sample was grown in the (100) plane, faceting in multiple directions had developed on the sample surface**.**

Figure 46: STM image 80nm x 80nm of (100) & (310) Terrace planes

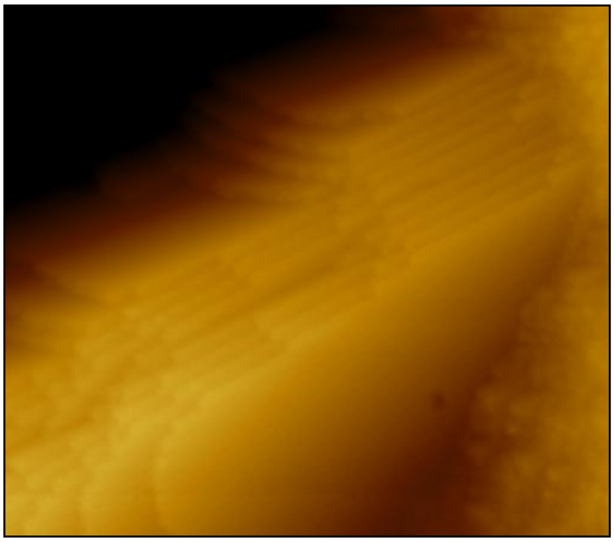

The following analysis confirms the presence of the (100) and (310) terrace planes, examining the profile of the surface, atomic spacing and surface symmetries, drawing comparisons between these measured quantities and the those expected theoretically. Despite the lack of atomic resolution, conclusions are drawn as to the existence of large scale atomic clusters on the sample surface, providing evidence for a preference of surface cluster formation on Ag-In-Gd, in certain Miller planes.

4.1.3 (100) plane

The formation of the (100) plane, located in the upper left hand corner of Figure 42, was to be expected as the sample was grown in the (100) plane. Analysis of the surface provides strong evidence the terrace is orientated in this direction, with atomic spacing, step height and surface symmetry consistent with the theoretical model.

4.1.3.1 Unit Cell

Observation of the square surface cell is consistent with the Ag-In-Gd sample being grown in the (100) direction. In *Figure 47* this square cell is displayed. The cell is made from the clusters preserved on the surface, therefore any comparisons made with the model should be made with the shape and spacing of entire clusters in the required direction.

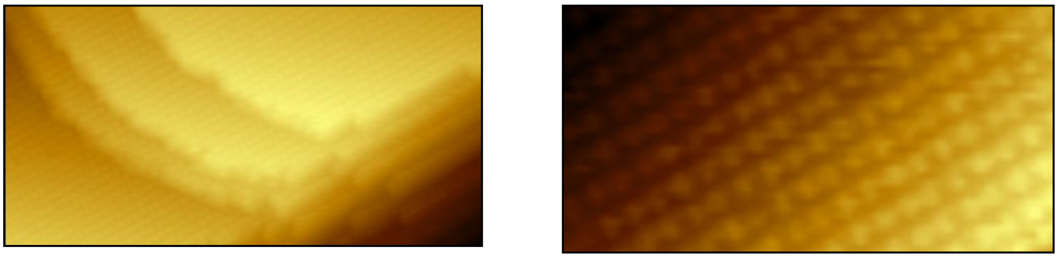

Figure 47: 80nm x 80nm image of surface terrace in the (100) plane, Figure 48 25nm x 25nm STM image displaying square unit cell.

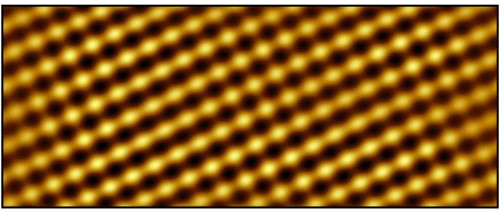

Figure 49: FFT of (100) terrace displaying periodic square surface cell

An FFT of *Figure 47* confirms the square unit cell periodicity of the clusters in the terrace. This square unit cell is consistent with the 2D model orientated in the (100) direction. The spacing between cluster centres in

***Figure 49* is 1.54nm**.

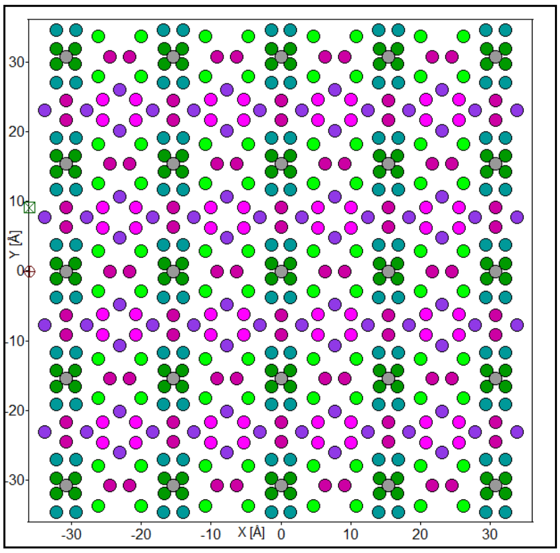

Figure 53:(100) Ag-In-Gd model,

4.1.3.2 Spacing

Due to the square cell observed on the surface of the (100) terrace, equal spacing is expected between clusters. Multiple profiles of the terrace were taken along the lines of cluster formation with an example displayed in *Figure 54*.

The length of the profile is then divided by the number of clusters through which it passes, to provide a cluster separation. Multiple measurements produced an average cluster spacing of (1.5 ±0.2) nm, which is consistent with the model in which the cluster spacing was 1.54nm. These measurements were repeated to a magnified area of the data.

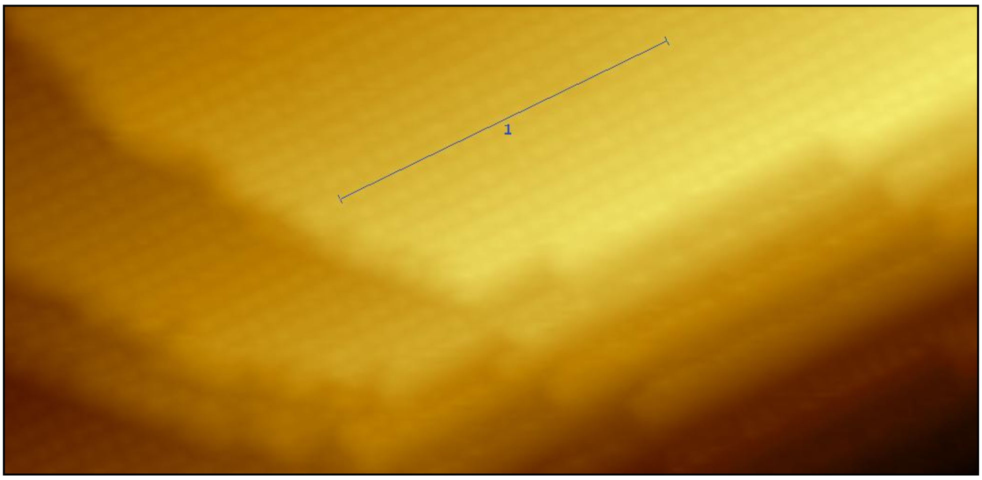

Figure 50: Profile over multiple cluster unit cells on (100) terrace
Figure 51: Surface model in the (100) plane

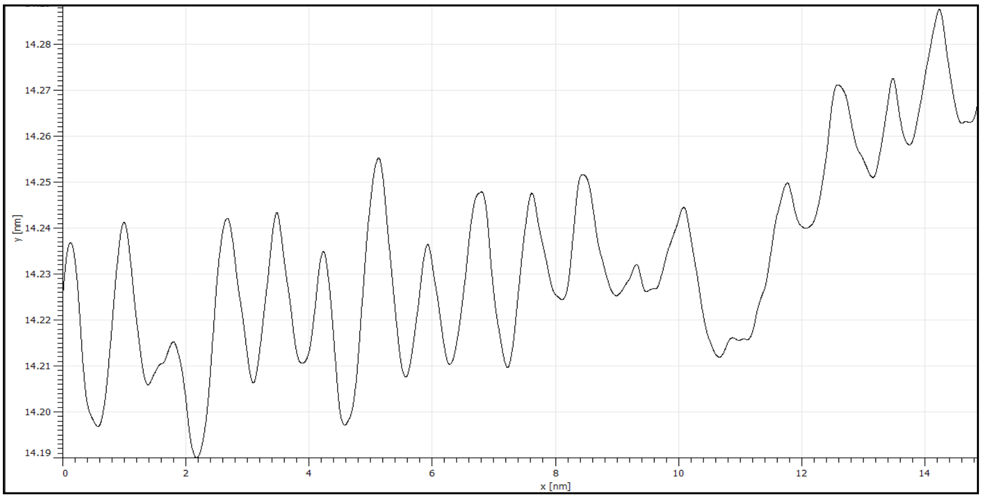

Figure 52: Length profile of (100) terrace, 10.38/7=1.482nm

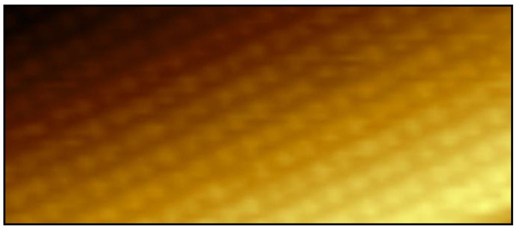

Figure 54Profile of the (100) terrace

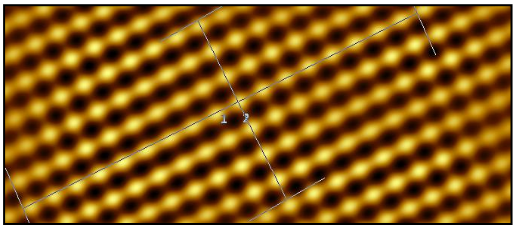

Figure 55: Profile taken across FFT of the (100) surface

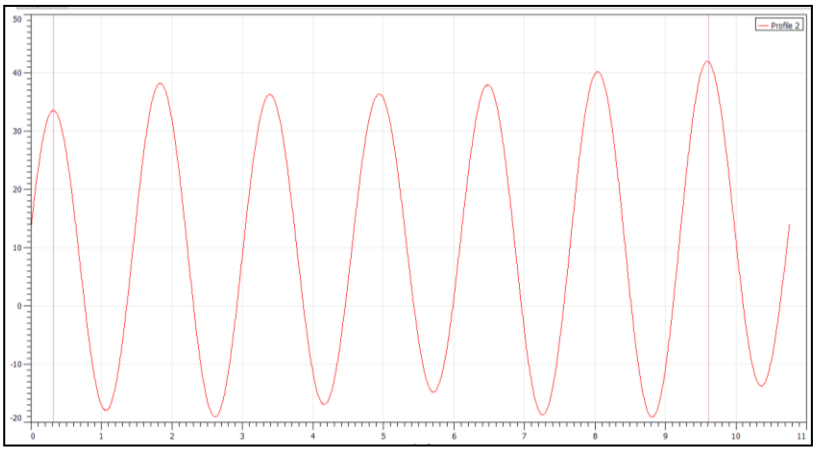

Figure 56: Plot of surface profile (100) terrace, X vs. Y (Å), spacing of 9.29/6=1.548nm

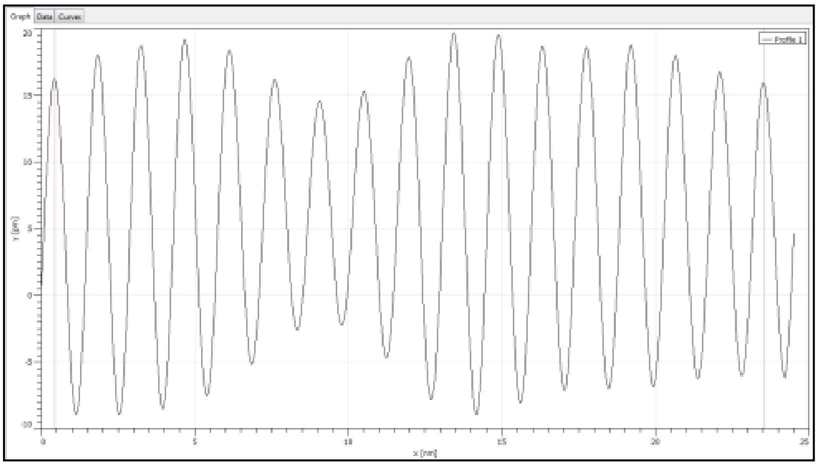

Figure 57: Plot of FFT surface profile, 23.07/15=1.538nm

After performing multiple profile measurements on the magnified image and an FFT of the image with improved periodicity, a value of cluster spacing of (1.5±0.2) nm was calculated.

4.1.3.3 Step height

As theoretically the Ag-In-Gd sample is BCC in structure, any step terrace should have a height of half the unit cell spacing i.e. 0.77nm. The clusters that are imaged on the surface appear to be positioned across square unit cells.

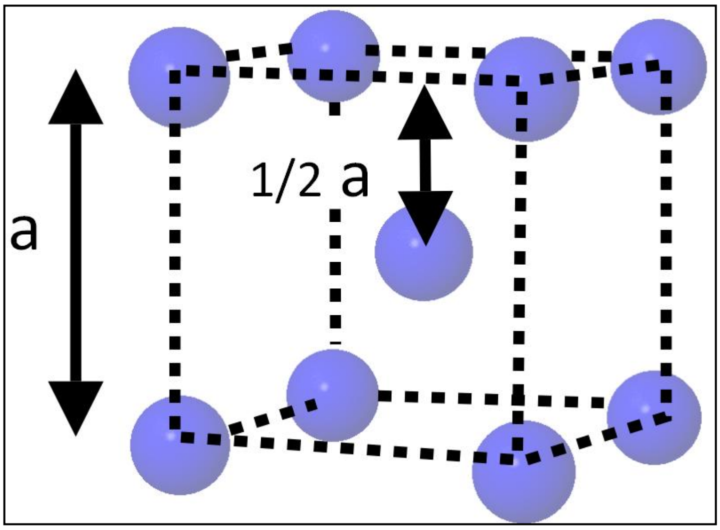

Figure 58: Half step spacing in BCC lattice

The observation of a step height close to 0.77nm would provide further evidence that the clusters are positioned upon the lattice points of two interlocking simple cubic cells, forming BCC lattice structure.

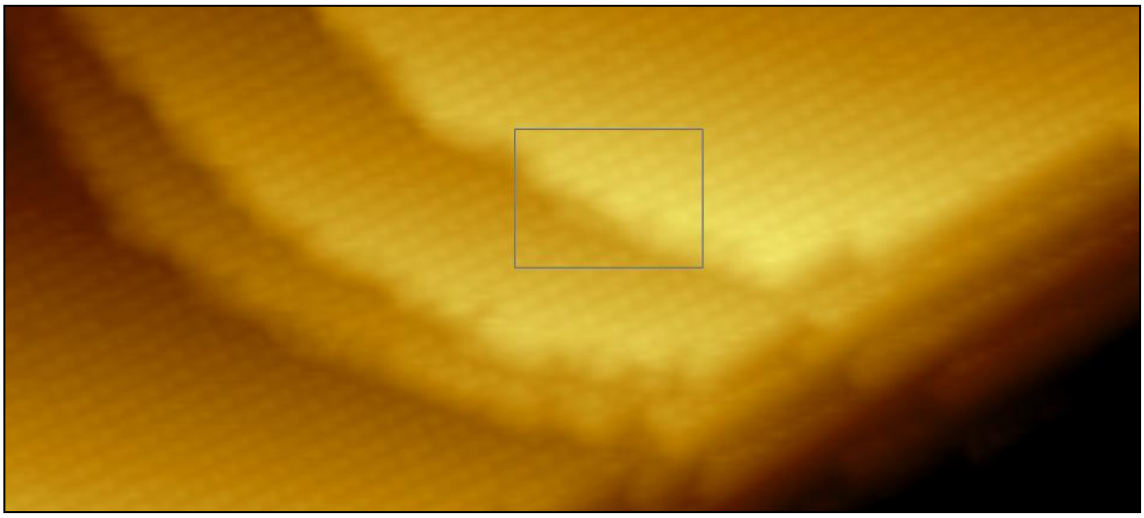

Figure 59: Density of atomic heights measured35 nm x 20nm

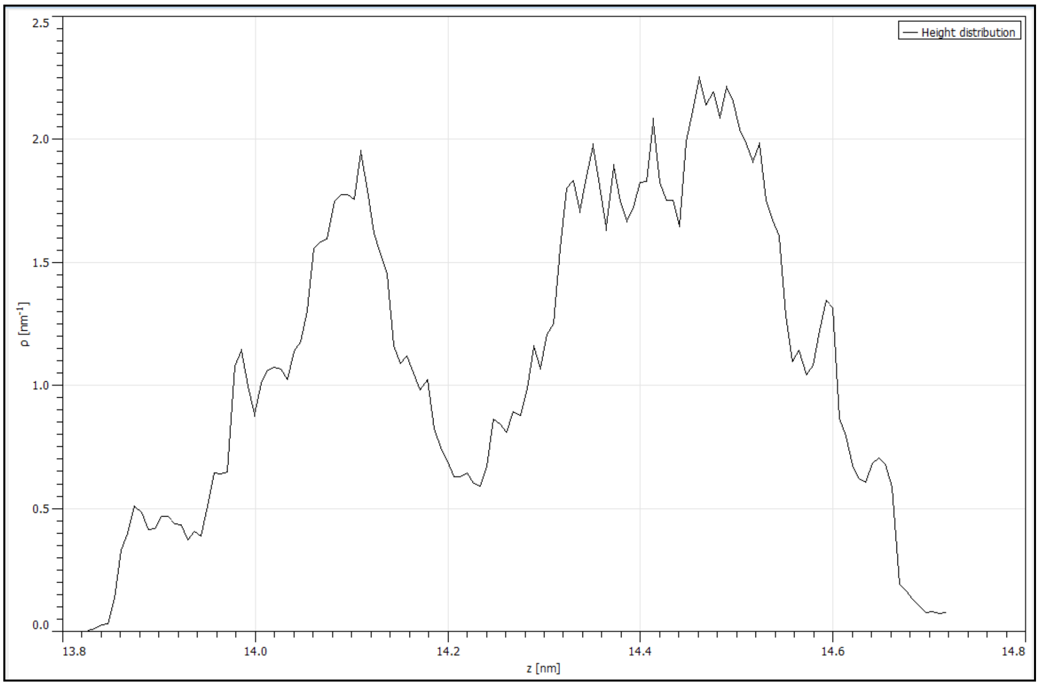

Figure 60: Histogram of step heights. 14.48nm-14.41nm=0.7nm

Figure 60 shows the distribution of the Z position of the atomics clusters, spaced across the two terraces highlighted in *Figure 61*. This is plotted against the density^{-1}nm. By taking the difference in the two peaks associated with each step, the step height is produced, with the error given as the variance of each peak. The step height in this case was calculated to be (0.7±0.1) nm. As the data did not contain any higher resolution images of the (100) plane, it was difficult to confidently measure the step height to a good degree of accuracy. The step edges appear to increase in height when compared with the centre of the same terrace. This has a significant effect on the average Z position of the clusters upon narrow terraces. However, to provide an indication that the step height is consistent with the model, a step profile was also measured.

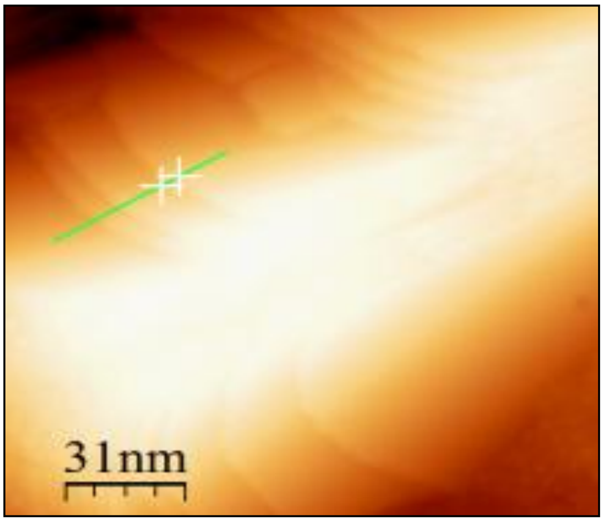

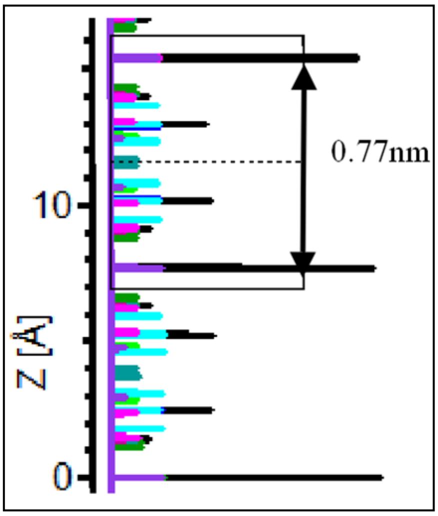

4.1.3.4

Figure 61: Step profile taken in the (100) plane

Figure 62: Spacing in Z of the high density atomic planes 0.77nm

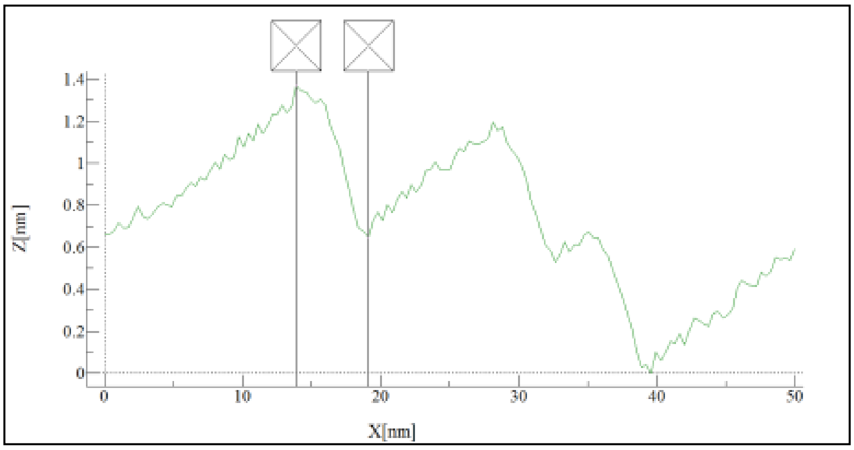

Figure 63: Step profile displaying a step height of 0.715nm

An example of the multiple profile measurements made between the two steps is displayed in *Figure 63*. The average difference in the Z position of the clusters between the two terrace levels was measured to be (0.7±0.1) nm. This can be used as evidence that the surface is consistent with the BCC structure seen in the model. This step height of approximately half of the unit cell spacing is also consistent with the spacing between high density atomic planes that are seen theoretically.

4.1.3.5 Inversion symmetry

Another defining characteristic of a BCC lattice structure is the inversion symmetry between terraces of different heights. As each new step is displaced by roughly half atomic spacing in the Z direction, the atomic rows, or in this case clusters, are positioned half a unit cell width either side of the adjacent terrace step. This is shown in the 3D model of Ag-In-Gd below in *Figure 64*.

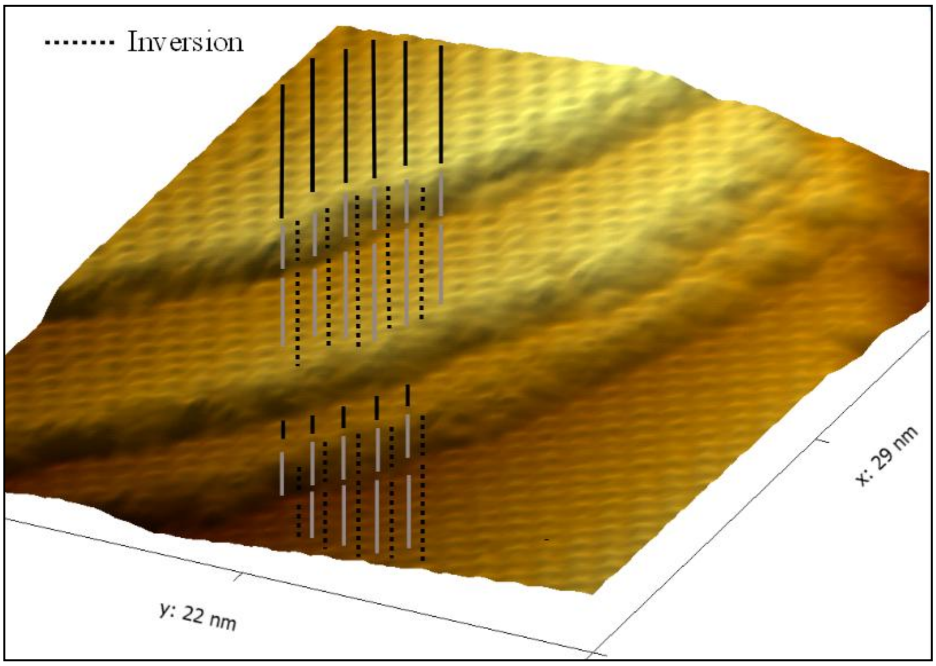

Figure 64: Inversion symmetry between the steps in the (100) Plane

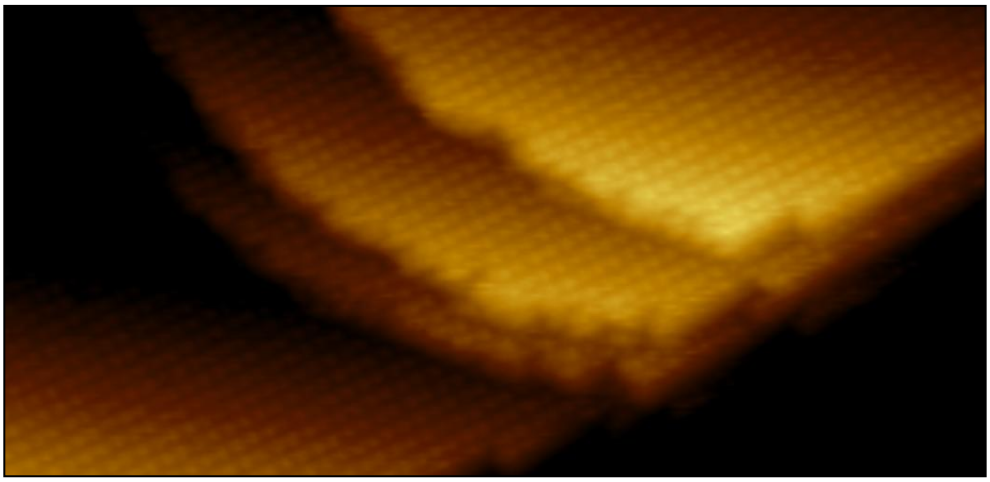

Figure 65: *Inversion symmetry between the steps in the (100) Plane*

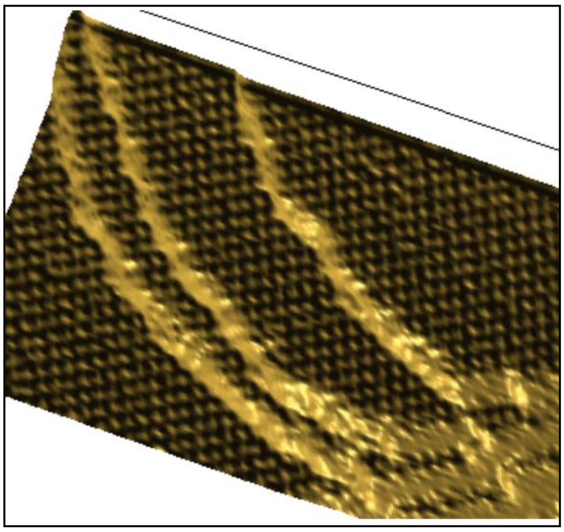

Figure 66: ***Inversion symmetry between the steps in the (100) Plane***

Figure 64 to Figure 66 show that inversion symmetry occurs between the different steps in the terrace. Not only does this provide further evidence that the surface and sample does indeed have a BCC structure, but due the limited scale resolution, it displays lattice positions decorated with icosahedral clusters, theoretically predicted for the Ag-In-Gd approximant. Further discussion of the presence of icosahedral clusters on the surface is given in the subsequent sections.

4.1.4 (310) plane

Analysis of the unidentified terrace (shown in Figure 67), has led to the conclusion that orientation is in the (310) plane. Justification for this statement is provided in the form of comparisons with the model, along with analysis of the angle formed between the two planes in the facet. Arguments of why the plane cannot be in the (110) or the (210) directions are also stated.

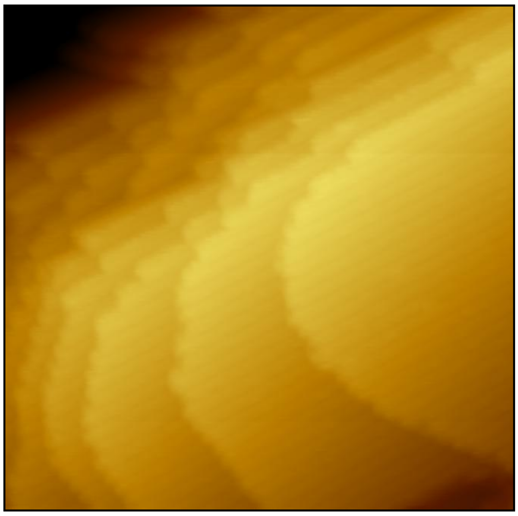

Figure 67: 80 nm x 80 nm STM image of the (310) terrace planes

4.1.4.1 Unit Cell

Higher resolution STM data was gathered for the (310) terrace, providing good images for analysis of the surface structure. A BCC structure, cut in the (310) plane, will provide a surface unit cell rectangular **(a x b)** in shape. In the case of our resolution, the clusters clearly adhere to this unit cell shape, visible in the STM shown in Figure 70.

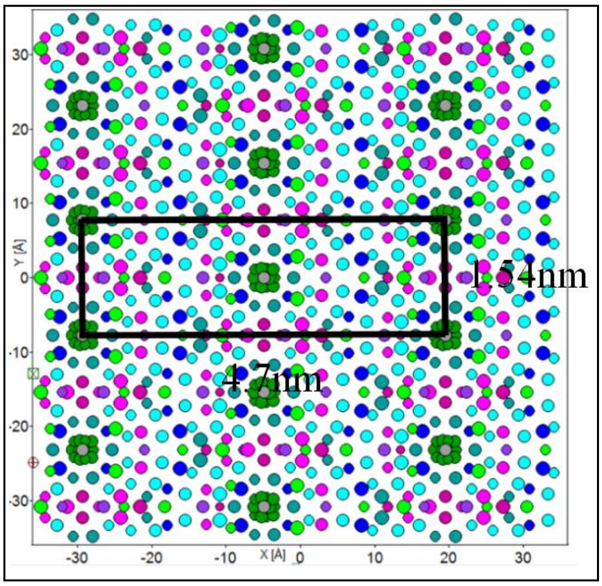

Figure 68: Rectangular unit cell of the (310) plane from bulk model

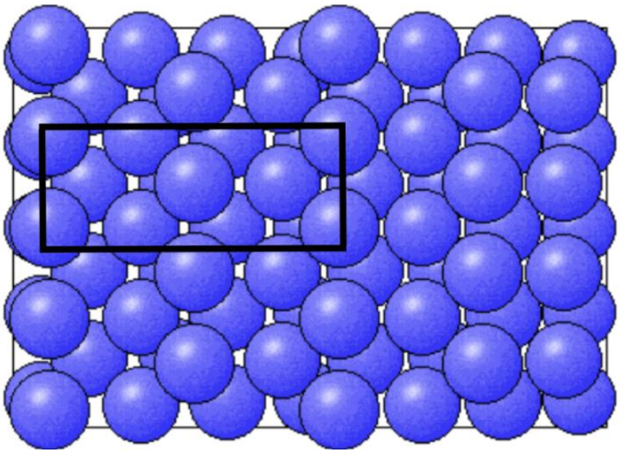

Figure 71: Surface model of the (310) unit cell

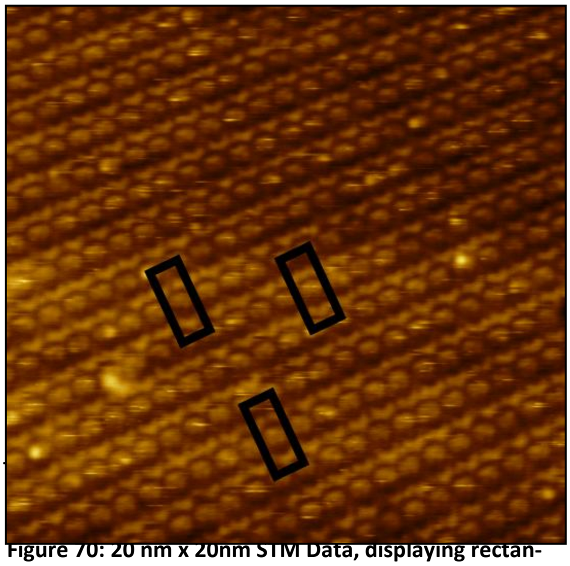

Figure 70: 20 nm x 20nm STM Data, displaying rectangular unit cell in the (310) plane.

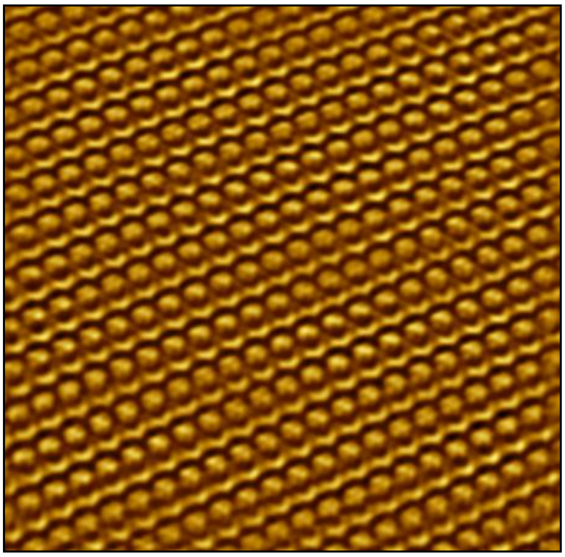

Figure 69: FFT of the (310) plane data.

An FFT of the (310) plane confirms this periodicity in which the unit cell cuts across one row of clusters. This is the first piece of evidence that rules out the (110) and the (210) planes in a BCC structure.

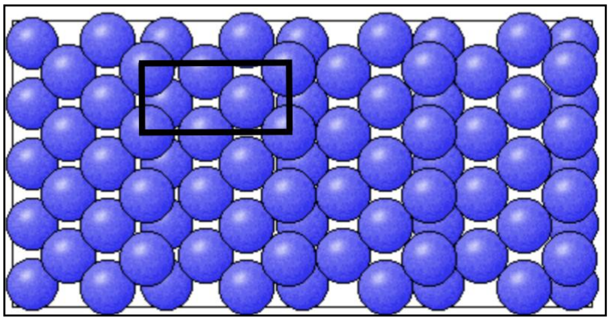

Figure 73:(210) surface model of unit cell

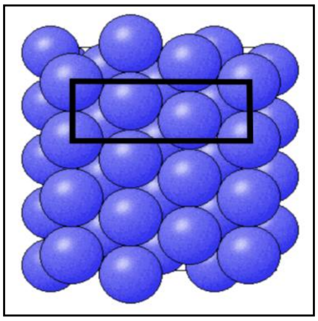

Figure 72:(210) surface model of unit cell

Models of the BCC (210) and the (110) clearly show the periodicity of the unit cell in these planes is inconsistent. The unit cell does not cut across the rows of clusters in the same way as shown in the data. The observation that the (210) surface is sparse, also suggests that a terraced formed in this miller plane is not favourable.

4.1.4.2 Spacing

A point to consider when analysing the unit cell spacing from the data, is the angle that the STM tip makes with the terrace plane. As the angle is non-zero, the measurement of length scales in the XY directions will be shorter than expected. This is illustrated in Fig 31.

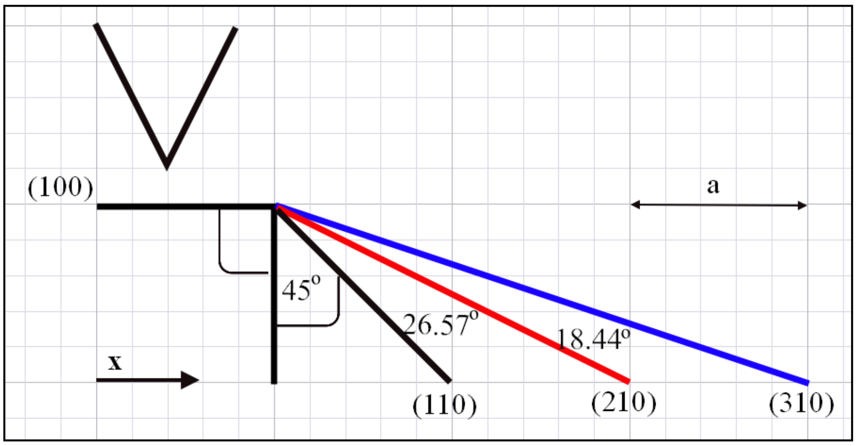

Figure 74: Distortion of STM measurements in XY plane

We can see here that when the tip travels a distance **√2 x a** along the (110) plane it will only measure a distance of **a** in the x direction. This should be accounted for when measuring the spacing between clusters in the data. This also rules out the (110) plane as the unit cell in the data for this terrace would appear identical to the unit cell in the (100), which is not the case.

It is also worth noting that the possibility that the terrace is in the (010) or (001) plane is ruled out by the fact that an angle of 90° to the (100) plane would be formed making imaging with the STM tip impossible.

As before multiple profiles were taken along the (310) plane, with example profiles shown in Figure 75 & Figure 76

4.1.4.3

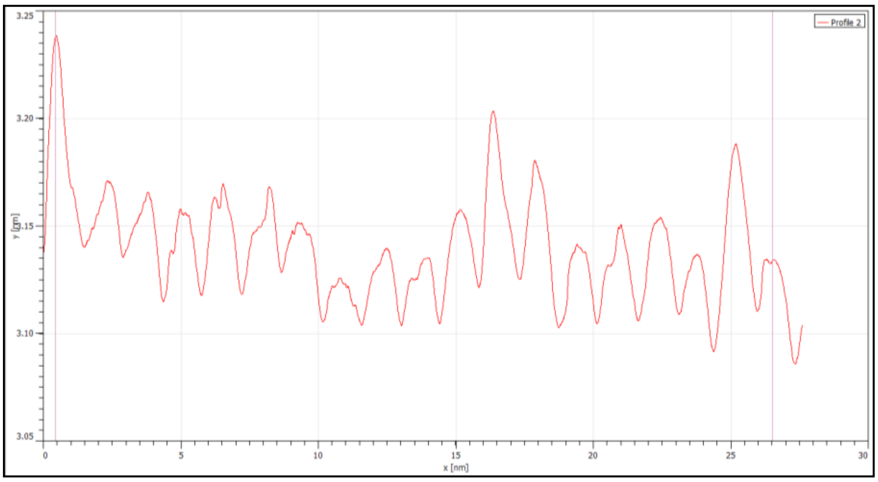

Figure 75: Length profile for a displaying spacing of 1.45nm

The unit cell spacing between clusters in **a** was measured to an average of (1.45±0.08) nm

4.1.4.4

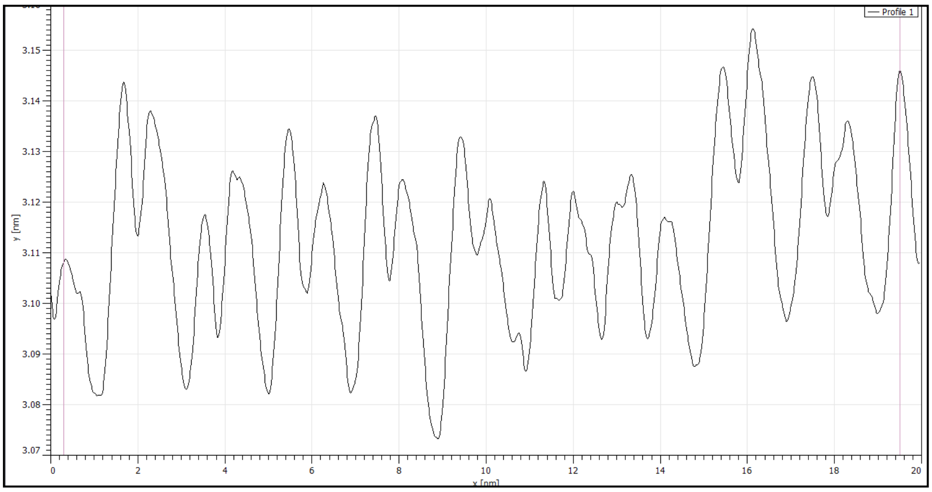

Figure 76: Length profile for b displaying spacing of 2.134 nm x 2 = 4.268 nm

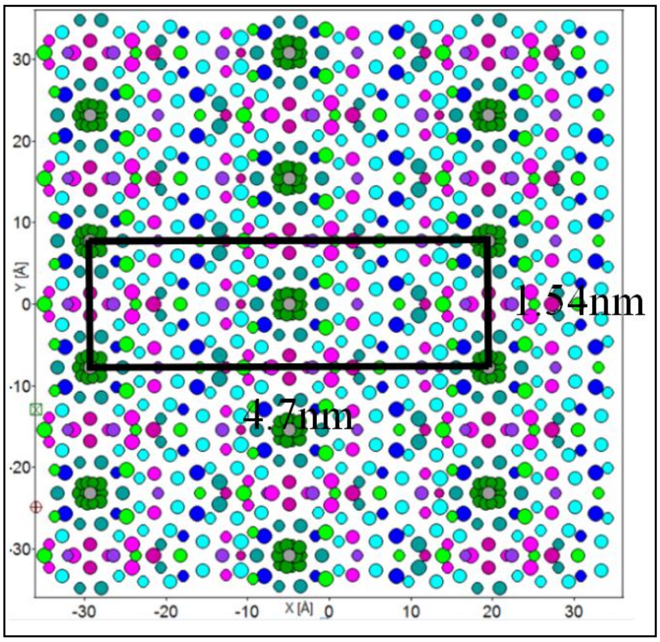

Figure 77: Rectangular unit cell from bulk model displaying lengths of sides a and b as 1.54 nm and 4.7 nm respectively

The average spacing between the cluster unit cells along **b** was measured to be (4.2±0.1) nm. When this is divided by Cos (18.44) to account for the angle made with the STM tip, the length becomes (4.5±0.1) nm, which compares well to the spacing in the (310) model of 4.7nm.

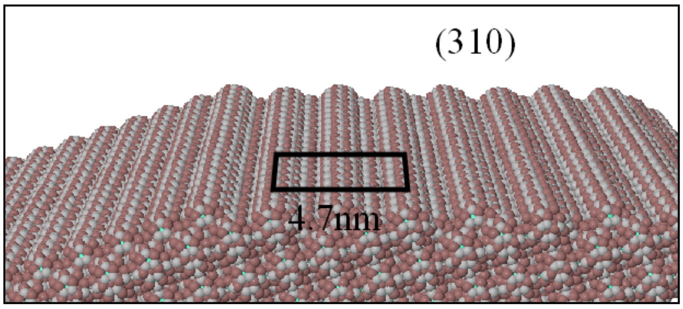

Figure 78: (310) plane in which clusters are preserved. Rectangular unit cell is again seen.

The combination of unit cell periodicity and dimension is shown in Figure 78, a 3D representation of the model, in which individual clusters have been added to each point on a BCC lattice. The characteristic cell span over two rows is consistent with this model.

4.1.4.5 Step Height

The step height was calculated to show the BCC structure was maintained in the (310) plane. Higher resolution data allowed a more detailed investigation of the terrace height possible. An example of the data used for this calculation is shown in Figure 79.

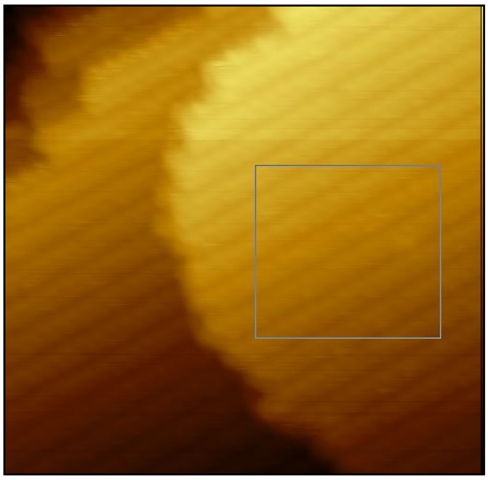

Figure 79: Upper Step height measured from (310) plane.

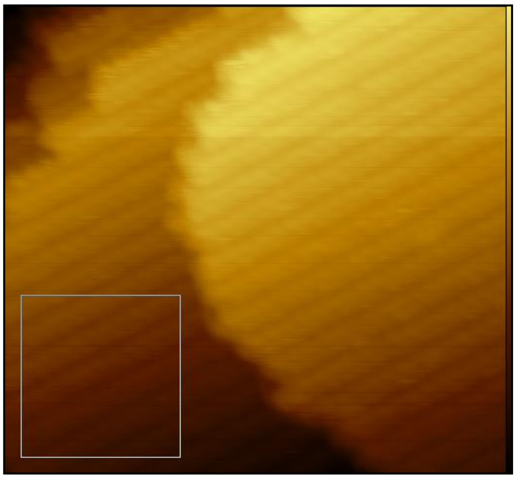

Figure 80: Lower Step height measured from (310) plane.

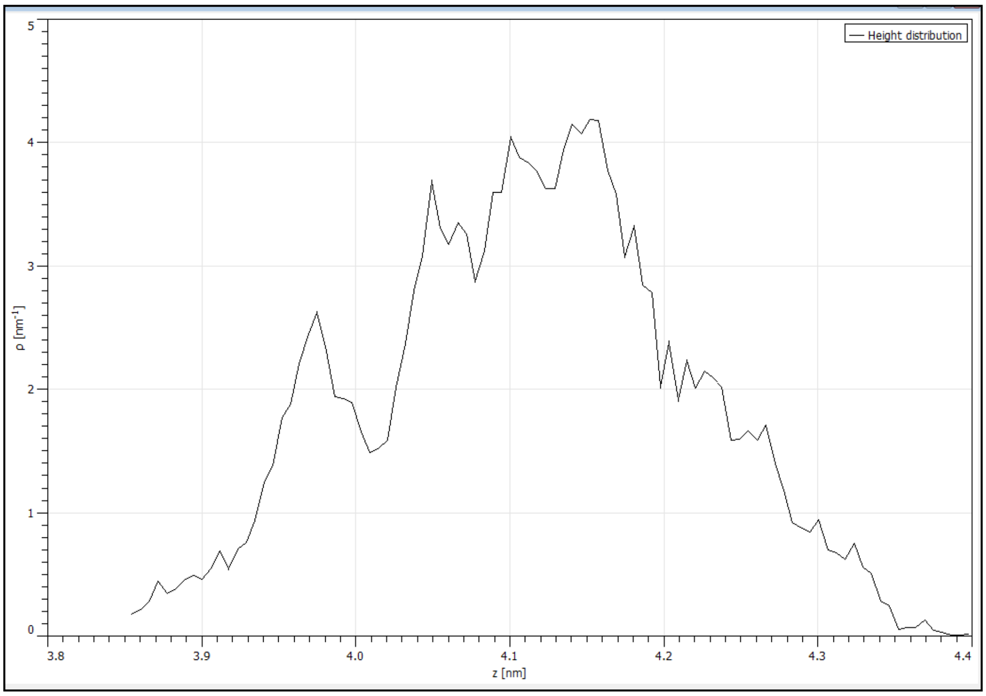

Figure 81: Histogram showing 4.12 nm to be the highest density Z position

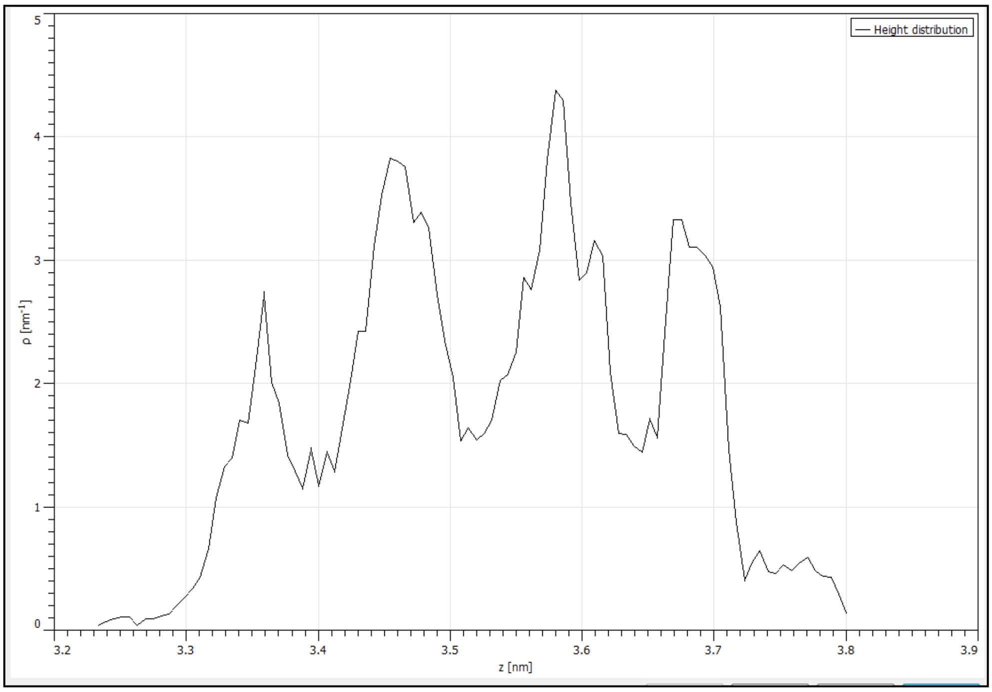

Figure 82: Histogram showing 4.12 nm to be the highest density Z position

The calculation of the step height in the (310) plane had to account for the offset in measurement due to the angle made with the STM tip. As a precursor, multiple samples of the cluster Z position were taken from each step. A histogram showing the most common heights at each step was generated as shown in Figure 81 & Figure 82. The mean value of (0.5±0.1) nm was calculated from the average difference in Z between each step. For a more complete analysis, the step profile was extracted from "Gwyddion" and adapted in Microsoft excel. As gwyddion only exports Z co-ordinates, the XY co-ordinates were generated to correspond to the image resolution (i.e. 40 nm x 40 nm ,512x512 Pixels).This set of data was then used to generate a 3D image of the steps on the (310) terrace as shown in Figure 83.

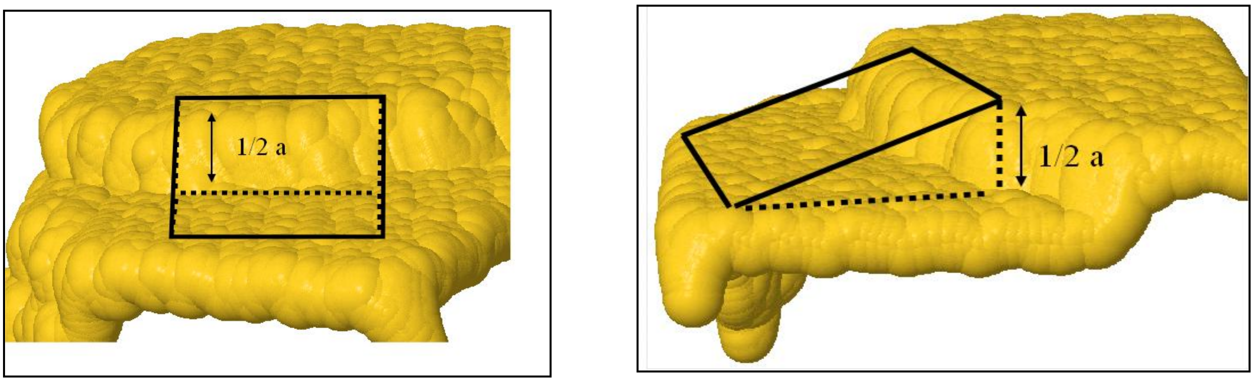

Figure 83 : 3D rendered image of STM (310) terrace data.

The Jmol image was then used to calculate the different step heights using simple trigonometry as shown above. The image could be manipulated in 3D without an error being induced due to the tip/plane angle, as the XY plane was generated in Microsoft excel and adjusted accordingly when rotations in 3D were made .The mean step height calculated was (0.74 ±0.09) nm. This is consistent with the model which shows high density planes every 0.77nm and is expected for a BCC structure,

4.1.4.6 Inversion symmetry,

As with the (100) plane, inversion symmetry is expected in the (31o). Figure 84 & Figure 85 display show this inversion symmetry between multiple steps in the terrace.

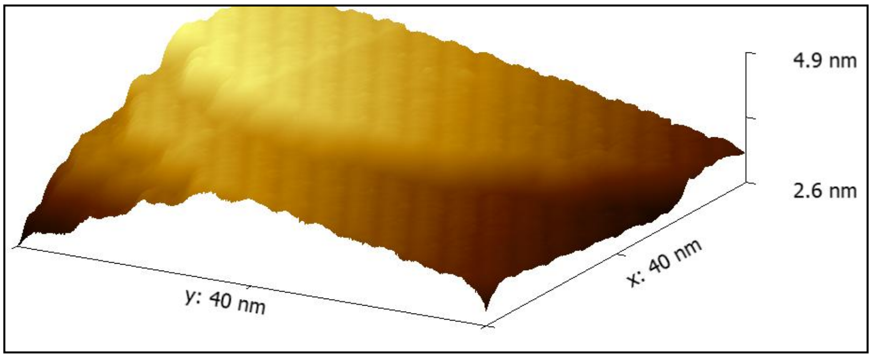

Figure 84: Inversion symmetry shown in (310) 3D rendered Image.

4.1.4.7

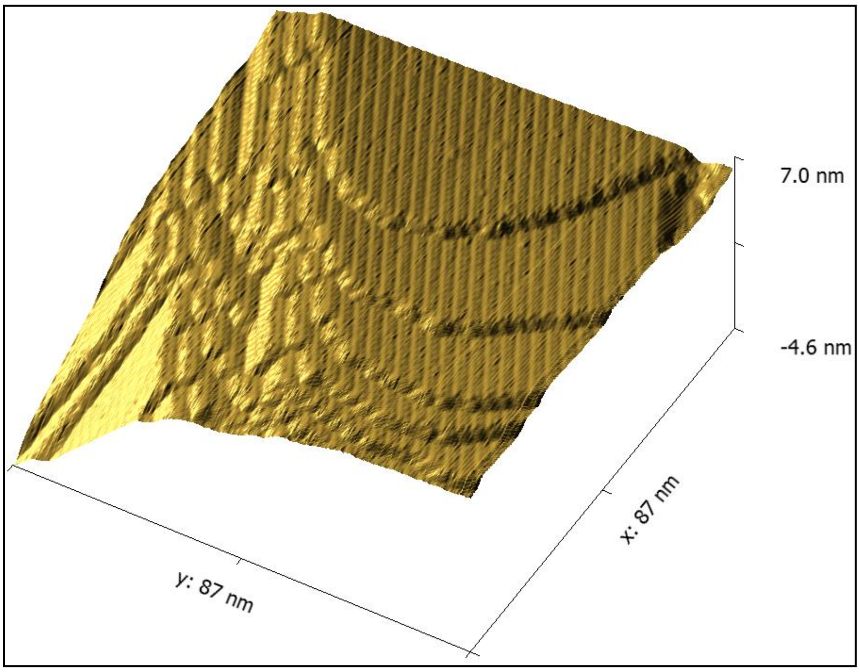

Figure 85: Inversion symmetry shown in (310) 3D rendered Image.

This is again consistent with a BCC structure cut in the (310) direction.

4.1.4.8 Angle between planes,

The strongest evidence that the terrace is indeed in the (310) Miller direction, comes from the angle that is formed with the (100) plane in the facet. Theoretically the angle should be 18.44°. This also makes it possible to rule out the (110) and the (210) planes. These would require an angle of 45° and 26.57° respectively as is shown theoretically:

$$cos\theta = \frac{h_1h_2 + k_1k_2 + l_1l_2}{\sqrt{h_1^2 + k_1^2 + l_1^2}\sqrt{h_2^2 + k_2^2 + l_2^2}}$$

Equation 4: Theoretical calculation of angle between Miller Planes (34)

$$(110)\ Plane : Cos\theta = \frac{1}{\sqrt{2}}, \qquad \theta = 45^{o}$$

$$(210)\ Plane : Cos\theta = \frac{2}{\sqrt{5}}, \qquad \theta = 26.57^{o}$$

$$(310)\ Plane : Cos\theta = \frac{3}{\sqrt{10}}, \qquad \theta = 18.44^{o}$$

After analysing the data the angle between the planes was calculated to be (18.1±1.2) degrees, which is consistent with the angle expected between the (100) and the (310), ruling out other possible planes. The calculation of this value is now discussed. Firstly, the equation of each plane is derived from cluster positions on each terrace and utilised to plot the vector normal to each plane.

Plane Equation:

$$Ax + By + Cz + D = 0$$

Equation 5: Equation of the plane (34)

Where the normal to the plane is the vector (ABC) as shown in Figure 86 & Figure 87

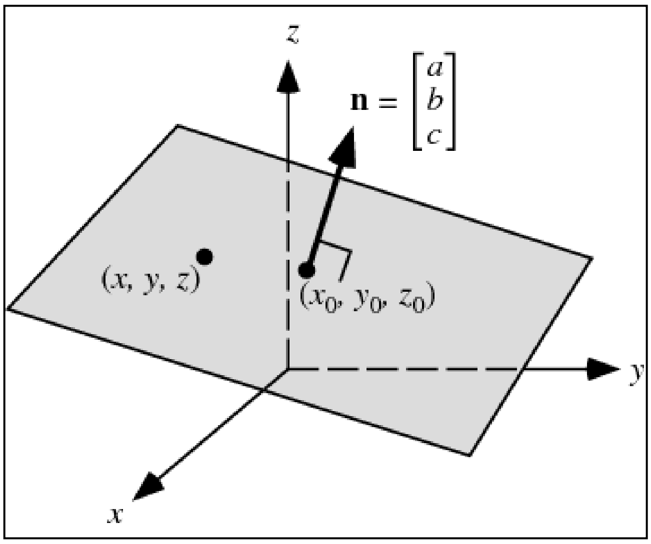

Figure 86: Vector normal to the plane (34)

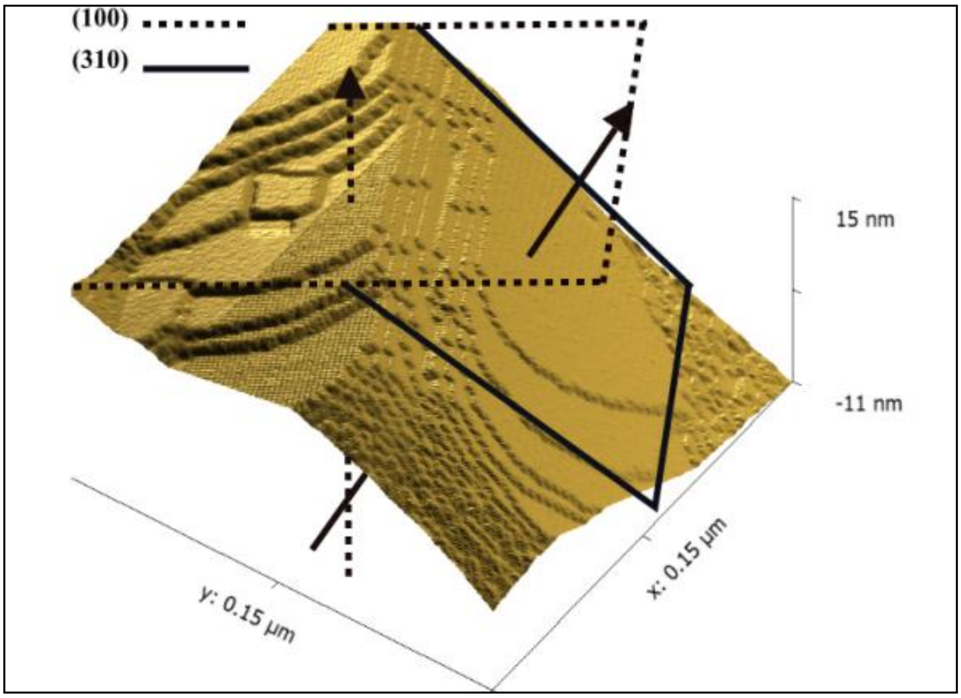

Figure 87:3D representation of vector normal in the (310) plane.

Given three points in space, $(x1, y1, z1)$, $(x2, y2, z2)$, $(x3, y3, z3)$, plane equation is calculated by finding the determinants:

$$A = \begin{vmatrix} 1 & y1 & z1 \\ 1 & y2 & z2 \\ 1 & y3 & z3 \end{vmatrix} \quad B = \begin{vmatrix} x1 & 1 & z1 \\ x2 & 1 & z2 \\ x3 & 1 & z3 \end{vmatrix} \quad C = \begin{vmatrix} x1 & y1 & 1 \\ x2 & y2 & 1 \\ x3 & y3 & 1 \end{vmatrix} \quad D = - \begin{vmatrix} x1 & y1 & z1 \\ x2 & y2 & z2 \\ x3 & y3 & z3 \end{vmatrix}$$

Equation 6: Determinant of equation of the plane, to calculate space co-ordinates of the vector normals.

Where,

$$\begin{aligned} A &= y1\ (z2 - z3) + y2\ (z3 - z1) + y3\ (z1 - z2) \\ B &= z1\ (x2 - x3) + z2\ (x3 - x1) + z3\ (x1 - x2) \\ C &= x1\ (y2 - y3) + x2\ (y3 - y1) + x3\ (y1 - y2) \\ -D &= x1\ (y2\ z3 - y3\ z2) + x2\ (y3\ z1 - y1\ z3) + x3\ (y1\ z2 - y2\ z1) \end{aligned}$$

Equation 7: Determinant of equation of the plane, to calculate space co-ordinates of the vector normals.

Giving the plane equation in the form:

$$A_1x + B_1y + C_1z + D_1 = 0$$

$$A_2x + B_2y + C_2z + D_2 = 0$$

Equation 8: Equation of the plane for terraces (100) and (310) respectively.

And producing the vector normal:

$$\boldsymbol{a} = (A_1, B_1, C_1)$$

$$\boldsymbol{b} = (A_2, B_2, C_2)$$

Finally, the cross product is taken between the vector normal, yielding the angle between the two planes.

$$|\boldsymbol{a} \times \boldsymbol{b}| = |\boldsymbol{a}|\ |\boldsymbol{b}| sin\theta$$

Equation 9: Cross product rule between two planes vectors to calculate angle between them (34).

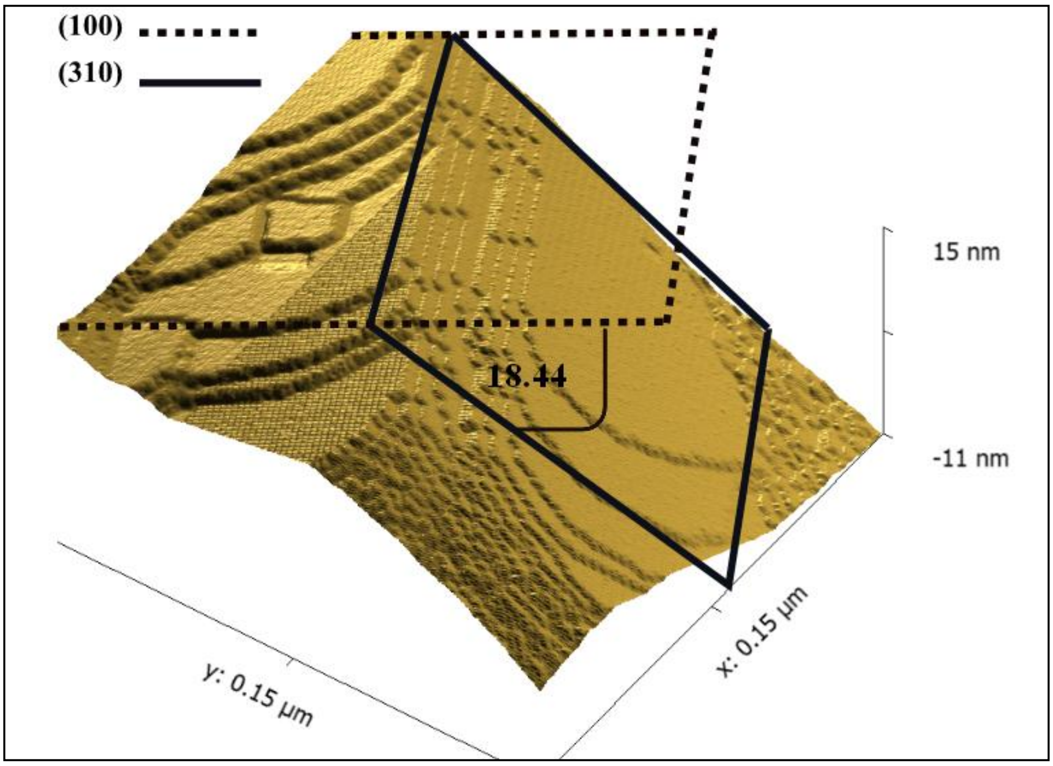

Figure 88: 3D representation of angle between (100) and (310) planes.

In practice the data was exported an scaled in excel to account for the tip/plane angle. Three random (xyz) cluster positions were selected from the (100) and three from the (310) terrace to generate each plane equation. The angle was calculated using the cross product method. This process was repeated using Microsoft excel to run the calculation multiple times (Table of results located in appendix), yielding an average angle between the planes of (18.0±2.4) degrees.

The analysis of the data so far has confirmed that the surface terraces are in the (100) and (310) direction, ruling out the possibility of different directions using the surface symmetries and angle between planes. However, so far there has been no consideration to how the symmetry of individual clusters, and the co-incidence of this symmetry with surface planes, may affect the faceting directions upon the surface. In the following section, the possible presence of the clusters upon the surface is discussed, along with the icosahedral structure of the individual clusters and how this may impact upon the plane of the terraces formed on the surface.

4.2 Possible Atomic Clusters Preservation

As previously discussed, the atomic clusters that decorate the BCC lattice of the Ag-In-Gd, approximant are thought to be imaged upon the sample surface. Imaging of these large scale structures is unexpected, as the clusters are normally unstable or “sliced through” during surface construction, to permit formation in the highest atomic density plane. The reader is referred to another case of possible cluster preservation upon a quasicrystal surface (6), in which large atomic clusters appeared to play a decisive role in the structuring of the Al-Pd-Mn quasicrystal. Interestingly, the preservation of the clusters at the surface would suggest in this case, that the usual preference for surface formation in high atomic planes is not seen .From this we may hypothesise that surface formation in this case arises in planes that correspond to symmetries within the atomic clusters. This hypothesis is now discussed, with the great need for further research and analysis kept in mind. Firstly, a comparison with the symmetry and structure seen theoretically in the atomic clusters with the STM data acquired from the Ag-In-Gd approximant sample will be made. The argument that the formation of the (310) terrace is due to the coincidence with the three-fold symmetries of the atomic clusters will be examined, with the same argument posed for the (100) surface but with evidence from LEED analysis.

4.2.1 Structure of Clusters

A single unit cell based around a cluster centre, was taken from the Shimoda model and built in three dimensions using Microsoft excel. Model clusters were then constructed by excluding atoms outside a certain radius from the cluster centre. This produced shells of atomic clusters which could be compared to other study of Ag based quasicrystal approximants, along with the STM data acquired from the Ag-In-Gd approximant sample. Ag-In-RE based quasicrystals are thought to have a Tsai type cluster (7). Due to this comparisons were made between these clusters and the clusters generated from the theoretical model.

An attempt to fit these shells to the adapted cluster model was made; however, it was first necessary to identify the shells made by various constituents of the cluster. The cluster shells calculated and built in 3D by adapting the Shimoda model in Microsoft Excel are shown in Figure 90

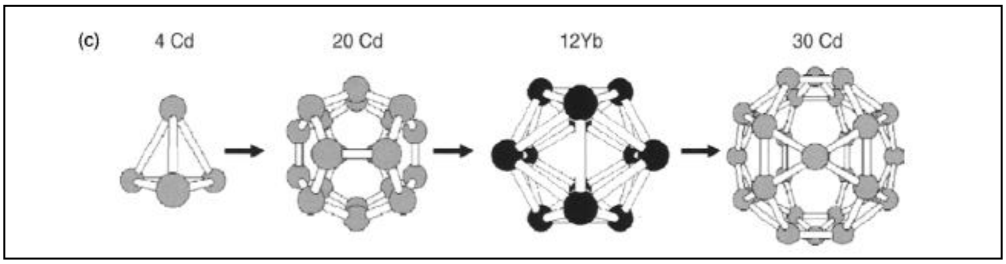

Figure 89: Tsai Type cluster, the centre is a Cd tetrahedron, the 1st shell is a Cd dodecahedron, 2nd shell is a Yb icosahedrons, and a 3rd shell is a Cd icosidodecahedron. （Alloys: A stable binary quasicrystal， 200）

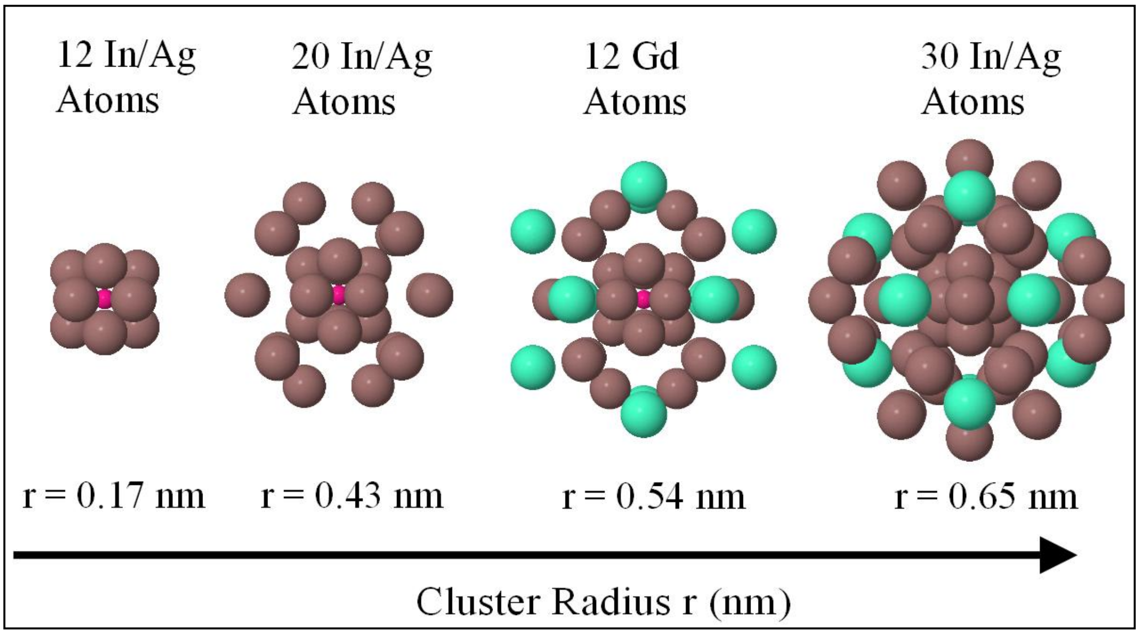

Figure 90: Atomic cluster Shells with increasing radius: 0.17 nm, 0.43 nm, 0.54 nm, 0.65 nm respectively.

This shell configuration adapted from the Shimoda model is consistent with the Tsai type cluster seen in Cd-Yb approximants, apart from the central cluster which is in this case icosahedral and not a tetrahedron in shape. The reason for this may be connected to the replacement of Cd with Ag-In.

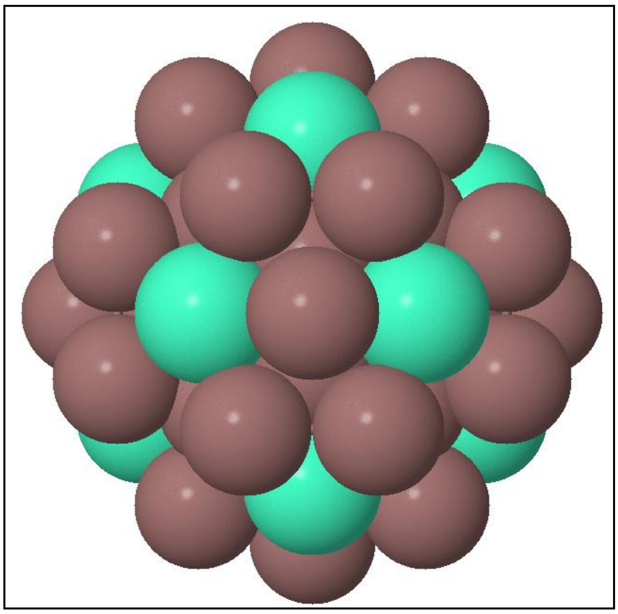

Figure 91: Icosahedral atomic cluster orientated in the (100) plane.

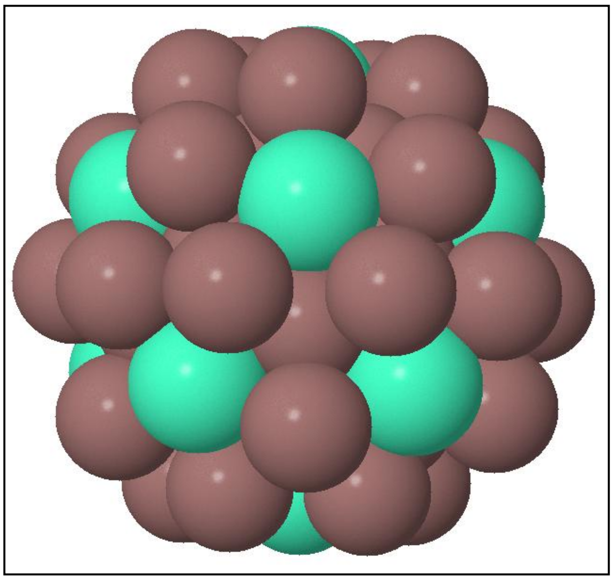

Figure 92: Icosahedral atomic cluster orientated in the (310) plane

The whole cluster of radius 0.65 nm is displayed in Figure 91 & Figure 92, orientated in the (100) & (310) planes respectively. From this the two-fold nature of the cluster can be seen in the (100) and the threefold nature of the cluster in the (310). It is reported that the total number of atoms in the cluster is 168 (35).However, comparison of the r = 0.65 nm cluster (containing only 74 atoms) with the data is appropriate, due to the coincidence of the terrace plane directions with the symmetries of clusters with this radius, as will now be discussed.

4.2.2 Co-Incidence with Cluster Planes

After establishing the class of cluster that the Shimoda model displays, it is possible to compare the co-incidence of the planes seen in the terraces with planes of the clusters. Clusters in the (310) terrace plane appear too coincide with the three fold symmetry of the icosahedral Gd shell (3rd shell from 3D model cluster Figure 90). The STM image in Figure 93, displays how the shape of the clusters in the row coincide with the three fold plane of the icosahedral clusters formed by gadolinium atoms. The triangle formed between three atoms can be identified upon each cluster marked below. This is consistent with the surface cluster model, in which the gadolinium atoms form the topmost layer of the cluster generated using the "VES-

TA” software. This coincidence with the threefold plane of the icosahedral cluster, may explain why the (310) plane has formed.

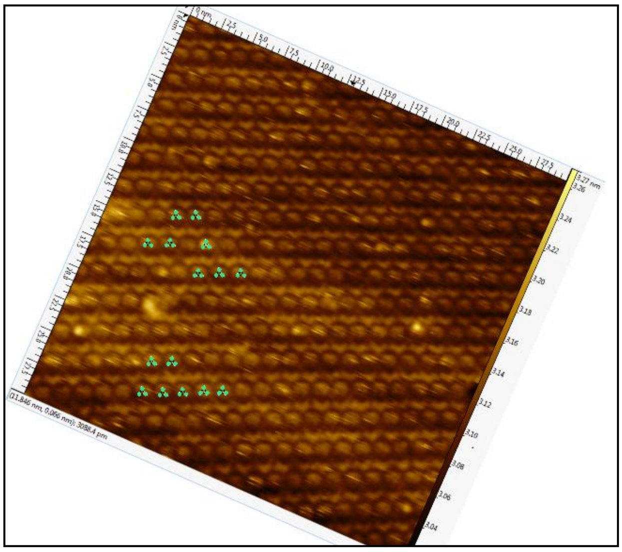

Figure 93: STM image of (310) Terrace displaying triangular face formed by Gd atoms in the icosahedral cluster

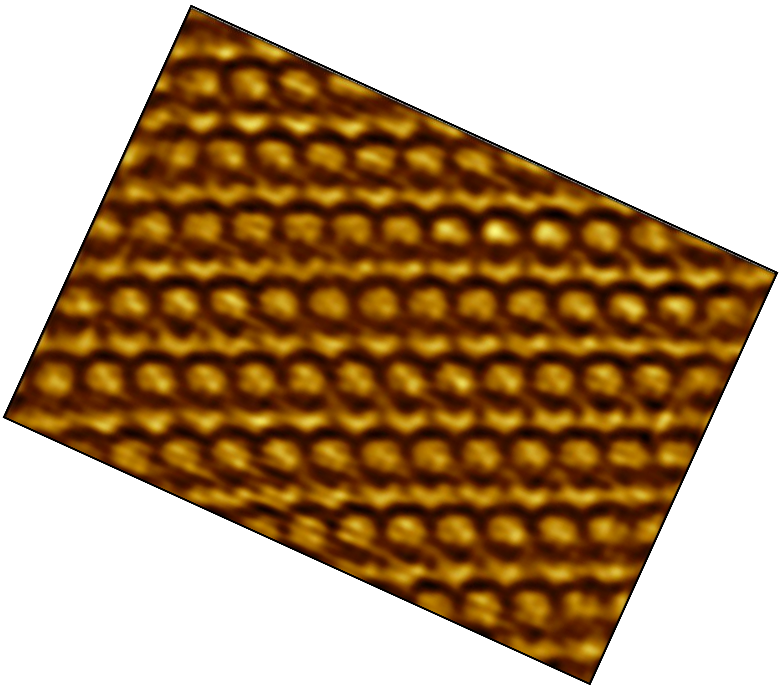

Figure 94: FFT of the (310) terrace displaying triangular face formed by Gd atoms in the icosahedral cluster.

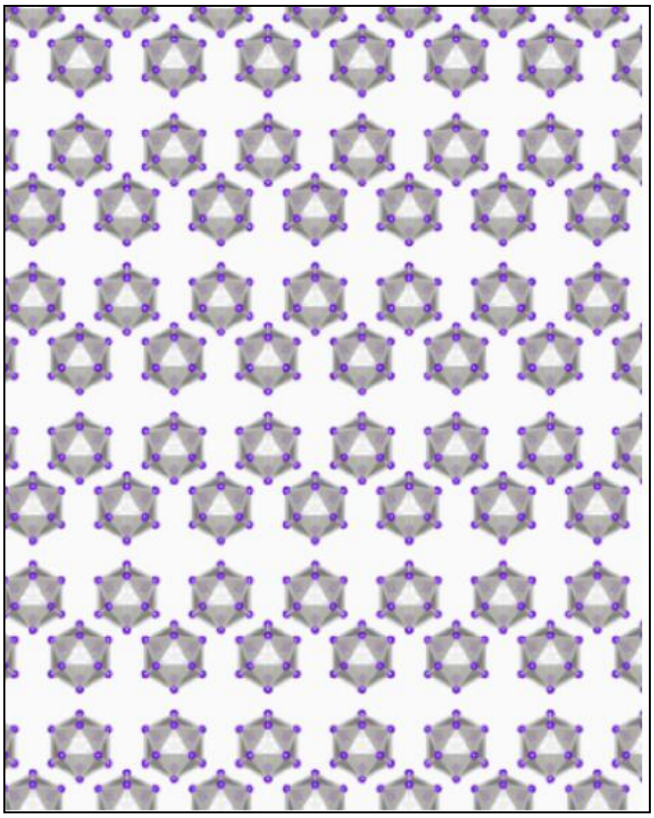

Figure 95: VESTA model showing topmost clusters only.

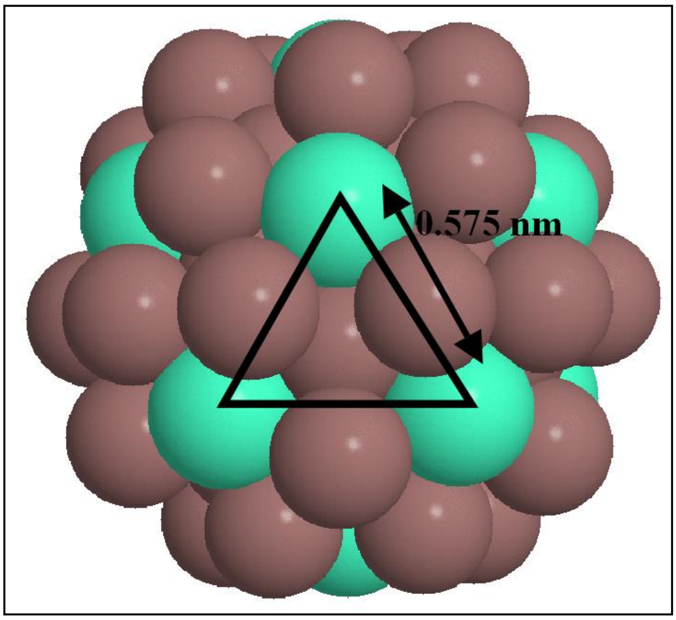

Figure 96: Edge spacing of triangular face

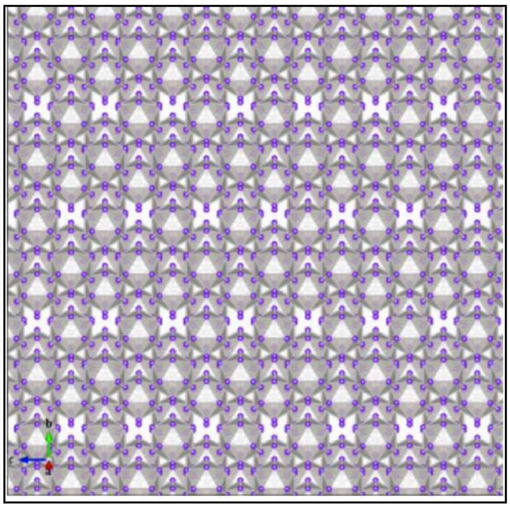

Figure 97: VESTA Model with clusters preserved.

The VESTA model, configured to preserve the clusters of the surface, shows that when the model is orientated in the (310) direction, the three fold, triangular shell face of the icosahedral Gd shell, forms the topmost layer. Furthermore, the edge length of the triangular face in this model icosahedral cluster (0.575 nm), is consistent with the edge length of the triangles highlighted in Figure 96 (0.54±0.06) nm from the (310) data clusters. Therefore, a conclusion can be drawn that the (310) plane is indeed coincident with the threefold triangular plane of the Gd icosahedral shell of the surface clusters. This would be in line with the original argument, that cluster preservation is taking place due to co-incidence with cluster symmetries. However, if this is correct, the co-incidence appears to be with the inner Gd shell of the atomic cluster, therefore only the inner shell of the clusters are preserved on the surface.

A similar method for the investigation of clusters on the (100) surface was used. If clusters are indeed preserved in the (100) plane, a rhombic unit cell would appear on the (100) plane, to coincide with the rhombic two fold plane of the icosahedral clusters. This is shown in Figure 97 & Figure 98, which displays the appearance of the clusters when preserved on the surface in the (100) plane, and the two-fold symmetry that would co-incide with the (100) plane.

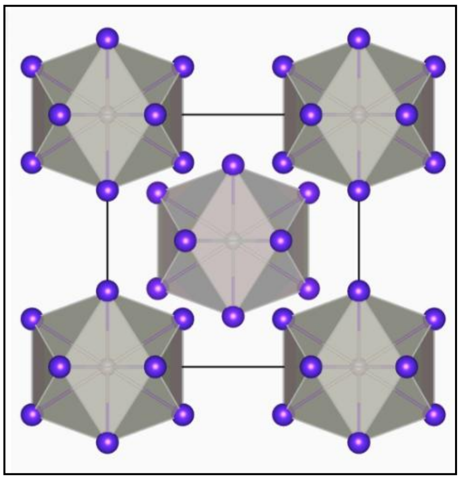

Figure 98: VESTA model showing cluster preservation and rhombic unit cell on (100) surface (32).

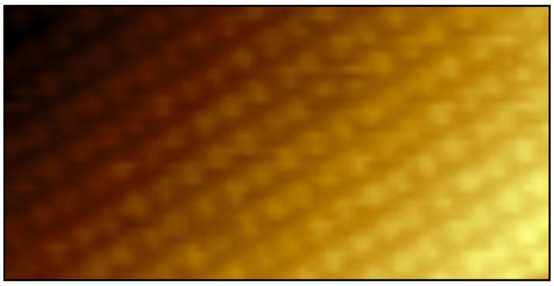

Figure 99: Square unit cell on (100) terrace not consistent with cluster preservation model, which predicts a rhombic unit cell.

We can see from Figure 99 that this rhombic surface cell is not present in the (100) data, which would rule out cluster preservation on the (100) surface. However, LEED analysis of the Ag-In-Gd approximant revealed a patter displaying rhombic symmetry. This is discussed in the following section.

To conclude, it appears that there is evidence for partial cluster preservation in the (310) plane. The co-incidence discussed is with the inner Gd shell of the cluster; specifically it’s three fold triangular face. This is still an extremely interesting result, as it confirms the possibility that, in this instance, the terrace may have formed due to planar symmetry within the icosahedral clusters. It is important to stress that repeated acquisition of STM data and analysis is required to further confirm this possibility.

4.3 LEED Analysis

The pattern obtained from LEED analysis shows distorted diffraction peaks over an energy range of 27eV to 41eV. This data is arranged in Figure 100

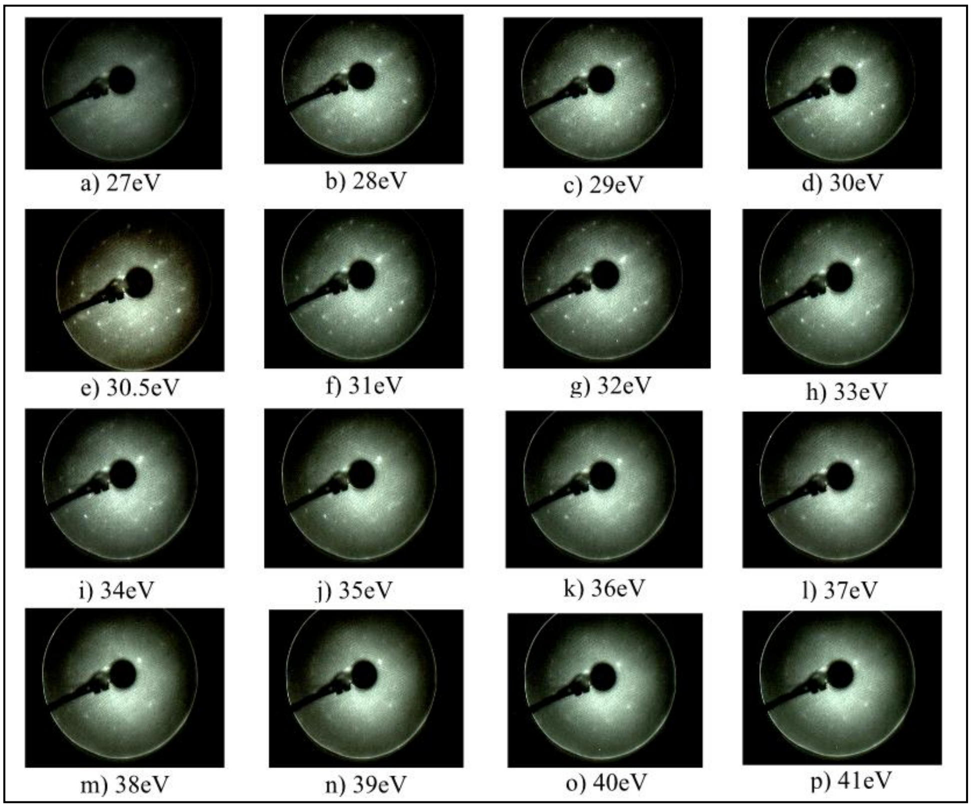

Figure 100: LEED diffraction patterns obtained within the energy range of 27eV-41eV

Unfortunately, due to time constraints using the equipment, data to calibrate the LEED apparatus was not collected, however some important points can be deduced from the results. The first observation to be made from the diffraction pattern is that certain peaks move towards a different specular. This is further evidence that there are facets formed on the surface. The clearest peaks were observed in the energy range 29eV-34eV. The spots that move towards a different specular are highlighted in Figure 101.

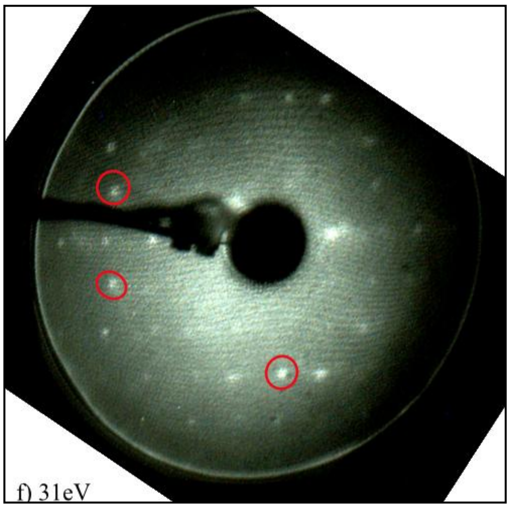

Figure 101: LEED diffraction pattern with energy 31eV

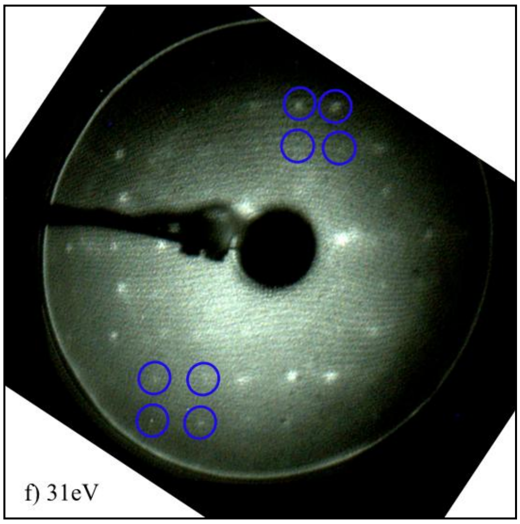

Figure 102: Square diffraction pattern from the long range cubic unit cell

The square symmetry of the cluster unit cells can be identified in the diffraction pattern, consistent with the cubic unit cell seen in the model for the (100) surface. These square unit cells are smaller features on the pattern, as the lengths displayed are in reciprocal space. Therefore they represent the long range cubic unit cell seen in the Ag-In-Gd approximant. Any larger spot features, belong to symmetries within the atomic clusters that are decorated periodically across the surface.

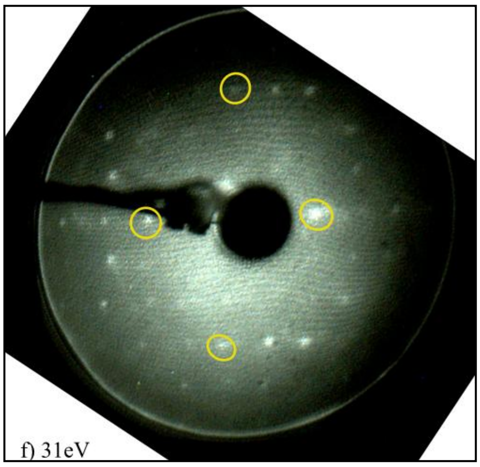

Figure 103: Rhombic symmetry originating from icosahedral cluster.

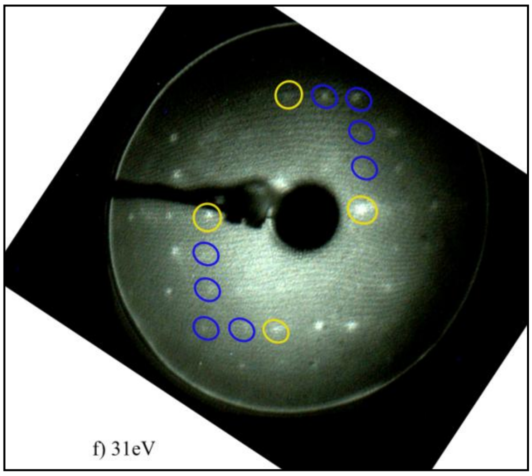

Figure 104: Edge length of rhombus seen in LEED pattern.

An atomic cluster feature of rhombic symmetry displayed by the electron diffraction peaks is shown in Figure 103. The rhombus spans 6 reciprocal unit cells in the y direction and 4 in the x direction as indicated on Figure 104. The spacing of the rhombus sides' **b*= √13 x a*** are calculated using the reciprocal relation:

$$\boldsymbol{a}^{*} = \frac{2\pi}{\boldsymbol{a}} = 4074698643$$

$$\boldsymbol{b}^* = \sqrt{13} \times \boldsymbol{a}^* = 12224095928m^{-1}$$

$$\boldsymbol{b} = \frac{2\pi}{\boldsymbol{b}^*} = \frac{2\pi}{12224095928} = 0.514nm$$

This is an interesting result, as it is similar to the edge spacing of the rhombic ,two-fold symmetry of the icosahedral clusters in the (100) direction as shown in Figure 60.

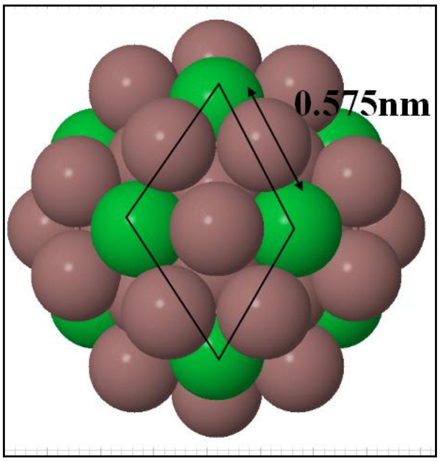

Figure 105: spacing along two fold edges in (100) orientated cluster.

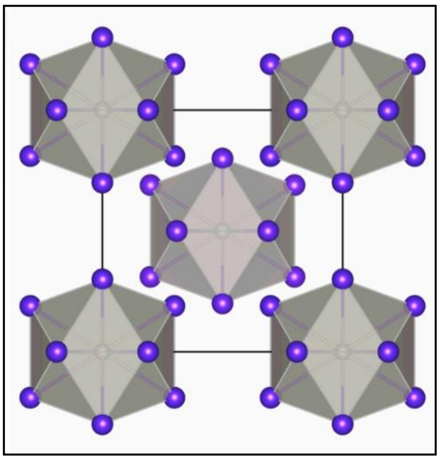

Figure 106: VESTA model in the (100) direction, with clusters preserved and displaying rhombic surface cell.

In this case, it appears that the rhombic shape displayed in the diffraction pattern, corresponds to the rhombic shaped face of the cluster seen in the (100) model plane. However, this is inconsistent with the STM analysis of the surface unit cell of the (100) terrace, as discussed in the previous section.

In summary, there is evidence that co-incidence with the triangular face of the preserved cluster s is seen in the (310) plane data. The rhombic unit cell expected from the STM data at the (100) surface was not imaged. Within the LEED diffraction pattern, this rhombic unit cell is seen, although contradicting the STM data. In summary, further investigation is required to resolve the inconsistencies between the STM data and LEED pattern of the (100) plane. The original argument that the (310) plane forms due to co-incidence with the three-fold symmetries of the atomic clusters is supported by the STM data.

5 Conclusion and Future Prospects

LEED and STM data were acquired from the Ag-In-Gd approximant sample. The imaging of facets via STM was consistent with the diffraction pattern produced whilst performing LEED. Successful comparisons were made between the theoretical model for the bulk Ag-In-Yb system and the structural units seen in the data from the Ag-In-Gd approximant. The BCC structure expected for the approximant was also confirmed, through the closer of surface terraces, present in multiple miller planes. It was established that the terrace planes were orientated in the (100) and (310) directions. The appearance of the (310) surface, coupled with the existence of facet planes that coincide with three-fold symmetries of the clusters, suggest the characteristic icosahedral clusters are preserved on the surface as was the case in the study of P.Ebert *et al* (6). Evidence to support this from the data was present but not conclusive. The initial aims of the experiment were met, with preparation parameters and useful data on from the structure of the sample surface taken. There are plans for the sample to be studied using X-ray diffraction techniques, in order to further confirm the sample is grown in the (100) miller plane. In conclusion, repetition of the experiment is now necessary, to obtain higher resolution STM data and reproduce the findings

6 Bibliography

1. *Structure of the fivefold surface of the Ag-In-Yb icosahedral quasicrystal.* **H. R. Sharma, M. Shimoda, K. Sagisaka, H. Takakura,J. A. Smerdon, P. J. Nugent, R. McGrath, D. Fujita,.** Surface Science Research Centre and Department of Physics, The University of Liverpool, Liverpool L69 3BX, United Kingdom : s.n., 2009, PHYSICAL REVIEW B , Vol. 80, p. Article:121401. 10.1103/PhysRevB.80.121401.

2. **J. A. Venables, Introduction to Surface and Thin Film Processes.** *Introduction to Surface and Thin Film Processes.* Cambridge : Cambridge University Press, 2000.

3. *A comparative study of the magnetic properties of the 1/1 approximant Ag-In-Gd and the I-QC Ag-In-Gd.* **PWang, Z M Stadnik, K Al-Qadi and J Przewo´znik.** Department of Physics, University of Ottawa, Ottawa, ON, K1N 6N5, Canada : s.n., JOURNAL OF PHYSICS: CONDENSED MATTER, Vol. 21 (2009) 436007 (10pp).

4. *Approximants in the Ag–In–M and Au–Sn–M (M = Ca or Rare Earth Metals) Systems.* **TSAI, Yoshiki MORITA and An Pang.** Department of Materials Processing, Graduate School of Engineering, Tohoku University, Sendai 980-8579, Japan : s.n., Japanese Journal of Applied Physics, Vols. Vol. 47, No. 10, 2008, pp. 7975–7979, p. 3.

5. *Quasicrystals and Crystalline Approximants.* **A. I. Goldman, R. F. Kelton.** 1993, Review of Modern Physics, Vols. Rev. Mod. Phys. 65, 213–230 (1993) , pp. 1-5.

6. *Evidence for a Cluster-Based Structure of AlPdMn Single Quasicrystals.* **Ph. Ebert, M. Feuerbacher, N. Tamura, M. Wollgarten, and K. Urban.** Institut für Festkörperforschung, Forschungszentrum Jülich GmbH, D-52425 Jülich, Germany : s.n., 28 OCTOBER 1996, PHYSICAL REVIEW LETTERS, Vols. VOLUME 77, NUMBER 18.

7. **Ishii, Takeo Fujiwara and Yasushi.** *Handbook of Metal Physics.* Tokyo : s.n., 2008.

8. *An introduction to the surface science of quasicrystals.* **Thiel, A.P.** 3-8, Department of Chemistry and Ames Laboratory, Iowa State University, Ames, IA 50011-3111, USA : s.n., April 2004, Progress in Surface Science, Vol. 75, pp. 2-4.

9. *Metallic Phase with Long-Range Orientational Order and No Translational Symmetry.* **D. Shechtman, I. Blech, D. Gratias, and J.W.Cahn.** PACS numbers: 61.50.Em, 61.55.Hg, 64.70.Ew, November 12, 1984, Phys. Rev. Lett. 53 (1984), pp. 1-4.

10. *Alloys: A stable binary quasicrystal.* **A. P. Tsai, J. Q. Guo, E. Abe, H. Takakura & T. J. Sato.** Nature 408, s.l. : Macmillan Magazines Ltd, November 30, 200, Nature, pp. 1-2. doi:10.1038/35046202.

11. **Dubois, Jean-Marie.** *Useful Quasicrystals:.* River Edge : World Scientific Publishing Co., 2005. pp. 1-30,360-380. 9789812567888.

12. *Thermal and electrical transport properties of Ag- In-Yb quasicrystals.* **Sivakumar, Y. K. Kuo and K. M.** Department of Physics, National Dong Hwa University, Hualien 97401, Taiwan : s.n., 2005, p. 1.

13. **R.A, Dunlap.** *The Golden Ratio and Fibonacci Numbers.* London : World Scientific Publishing Co.Pte.Ltd, 2003. pp. 1,24,25,26. 9810232640.

14. *A Guide to Mathematical Quasicrystals.* **Baake, Michael.** Institut fur Theoretische Physik, Universitat Tubingen,Tubingen, Germany : s.n., Jan 20, 1999, Cornell University Library, pp. 9,10.

15. *Quasicrystal surfaces: structure and potential as templates.* **R. McGrath, Julian Ledieu, Erik J Cox and Renee D Diehl.** R119-R144, Surface Science Research Centre, The University of Liverpool, Liverpool L69 3BX, UK : s.n., Jan 18, 2002, JOURNAL OF PHYSICS: CONDENSED MATTER, Vol. 14, p. 4. stacks.iop.org/JPhysCM/14/R119.

16. *Materials science: A tale of two tilings.* **Keys, Sharon C. Glotzer & Aaron S.** July 29, 2008, Nature, Vol. 424, pp. 420-421. doi:10.1038/454420a.

17. *Crystal and Quasicrystal Structures in Al-Mn-Si Alloys.* **Henley, Veit Elser and Christopher L.** 26, Murray Hill Laboratories, New Jersey, Usa : s.n., Dec 23, 1985, Physical Review Letters, Vol. 55.

18. **Luth, H.** *Solid Surfaces, Interfaces and thin Films.* s.l. : Springer, 2001.

19. *Synthesis of large single-grain 1/1 approximant crystals in the Ag–In–Eu system by the self-flux method.* **Tsai, Can Cuiab and An Pang.** Institute of Multidisciplinary Research for Advanced Materials, Tohoku University, : s.n., July 21, 2010, Philosophical Magazine, Vols. Vol. 91, Nos. 19–21, 1–21.

20. *Crystal Structure of Ag7-Mg26-ABinary Alloy Phase of the Mackay Cluster.* **Spiekermann, Guido Kreiner and Stefan.** 2001, Z.Anorg.Allg.Chem.2001,627,, Vol. 627, p. 24602468.

21. **Sharma, H.R.** Electron Diffraction - LEED. *Surface Science Lecture Course: Lecture 5.* Jan 2011.

22. **John Wiley and Sons.** *Surface Analysis:The Principle Techniques.* [ed.] John C.Vickerman. Chichester : Wiley, 2004. pp. 314-339.

23. **Sergei N. Magonov, Myung-Hwan Whangbo.** *Surface Analysis with STM and AFM.* New York : VCH, 2002.

24. **Prof.Nichols.** Chemical Nanotechnology: Lecture 9 STM . *Chemical Nanotechnology Lecture Course.* The University of Liverpool : s.n.

25. **Chen, C. Julian.** *Introduction to Scanning Tunneling Microscopy.* s.l. : Oxford Scholarship Online, 2007. p. Chapter 2. ISBN-13: 9780199211500.

26. **Elsevier.** *Methods in Experimental Physics.* [ed.] Joseph A. Stroscio and William J. Kaiser. s.l. : Elsevier, 2012. p. Chapters 2 & 3. Vol. 27.

27. **Sharma, H.R.** Surface Science Lecture Course - Surface Studies Lecture 3. *UHV Systems.* Liverpool, UK : s.n., Jan 2011.

28. *Step-terrace morphology and reactivity to C60 of the five-fold icosahedral Ag–In–Yb quasicrystal.* **P.J. Nugent, J.A. Smerdon, R. McGrath, M. Shimod, C. Cuib, A.P. Tsai and H.R. Sharma.** 19-21, Surface Science Research Centre and Department of Physics, The University of Liverpool. : Taylor & Francis, 2010, Philisophical Magazine, Vol. 91.

29. *First UHV surface studies of single-grain icosahedral Ag–In–Yb quasicrystal.* **HR Sharma, M. Shimoda,S. Ohhashi,A. P. Tsai.** 18-21, 2007, Philosophical Magazine, Vol. 87, pp. 2989-2994.

30. **Thiel, Patricia A.** 59, 2008, Annu. l Rev. Phys. Chem., pp. 129-144. 10.1146/annurev.physchem.59.032607.093736.

31. *Structure and reactivity of Bi allotropes on the fivefold icosahedral Al–Pd–Mn quasicrystal surface.* **J. A. Smerdon, N. Cross, V. R. Dhanak, H. R. Sharma, K. M. Young, T. A.Lograsso, A. R. Ross, and R. McGrath,.** 2010, Journal of Physics: Condensed Matter, Vol. 22. Article 345002.

32. **Shimoda, M.** Bulk Model for Ag-In-Yb Approximant. National Institute for Materials Science, 1-2-1 Sengen, Tsukuba, Ibaraki 305-0047, Japan : s.n.

33. **I. Horcas et al., Rev. Sci. Instrum. 78, 013705 (2007).**

34. **Weisstein, Eric W. "Plane." From MathWorld--A Wolfram Web Resource. http://mathworld.wolfram.com/Plane.html.** [Online]

35. **Tamura.** SSRC University of Liverpool, Quasicrystal Group Meeting 18/04/2012.

36. *Crystalline phases displaying pseudo-icosahedral symmetry in Ag-In-RE.* **J.F. Ruana, K.H. Kuo b,∗, J.Q. Guoc, A.P. Tsai.** 370 (2004) L23–L27, September 23, 2003, Journal of Alloys and Compounds.

37. *Materials science: A tale of two tilings.* **Keys, Sharon C. Glotzer & Aaron S.** July 29, 2008, Nature, Vol. 424, pp. 420-421. http://www.nature.com/nature/journal/v454/n7203/pdf/454420a.pdf . doi:10.1038/454420a.

7 Appendix

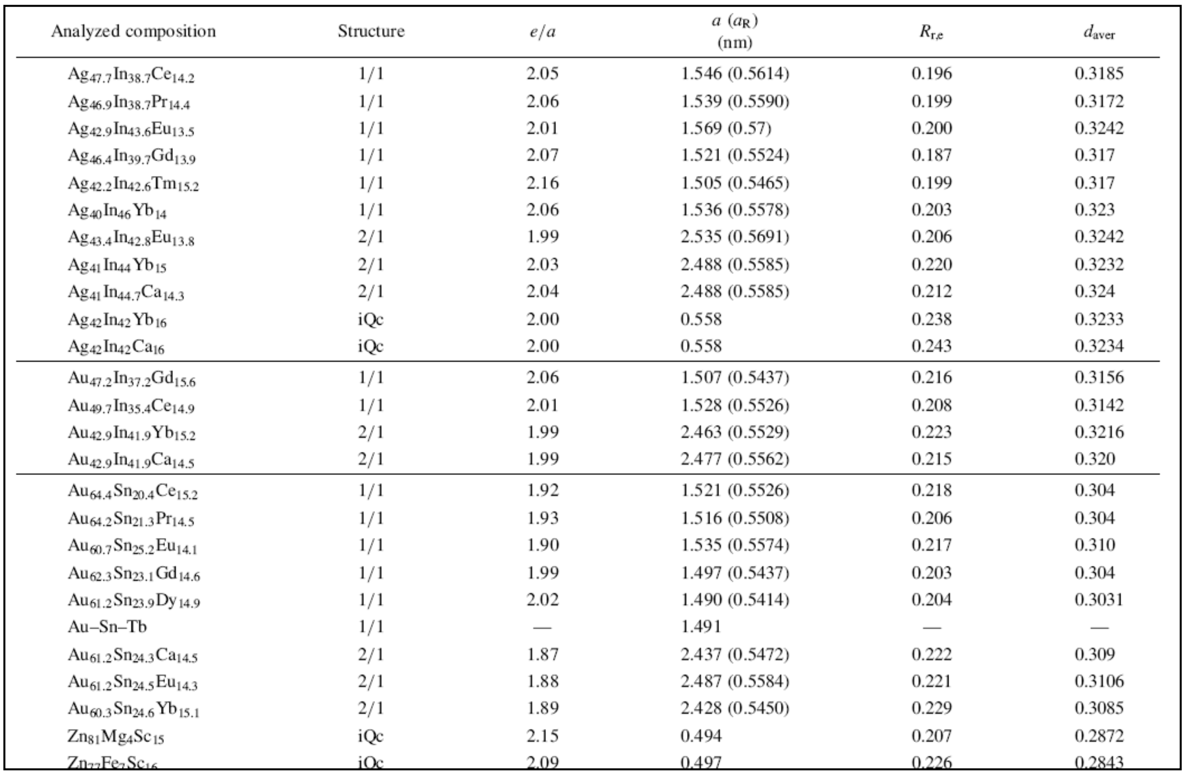

Analyzed composition	Structure	e/a	a (a_R) (nm)	$R_{r,e}$	d_{aver}
$Ag_{47.7}In_{38.7}Ce_{14.2}$	1/1	2.05	1.546 (0.5614)	0.196	0.3185
$Ag_{46.9}In_{38.7}Pr_{14.4}$	1/1	2.06	1.539 (0.5590)	0.199	0.3172
$Ag_{42.9}In_{43.6}Eu_{13.5}$	1/1	2.01	1.569 (0.57)	0.200	0.3242
$Ag_{46.4}In_{39.7}Gd_{13.9}$	1/1	2.07	1.521 (0.5524)	0.187	0.317
$Ag_{42.2}In_{42.6}Tm_{15.2}$	1/1	2.16	1.505 (0.5465)	0.199	0.317
$Ag_{40}In_{46}Yb_{14}$	1/1	2.06	1.536 (0.5578)	0.203	0.323
$Ag_{43.4}In_{42.8}Eu_{13.8}$	2/1	1.99	2.535 (0.5691)	0.206	0.3242
$Ag_{41}In_{44}Yb_{15}$	2/1	2.03	2.488 (0.5585)	0.220	0.3232
$Ag_{41}In_{44.7}Ca_{14.3}$	2/1	2.04	2.488 (0.5585)	0.212	0.324
$Ag_{42}In_{42}Yb_{16}$	iQc	2.00	0.558	0.238	0.3233
$Ag_{42}In_{42}Ca_{16}$	iQc	2.00	0.558	0.243	0.3234
$Au_{47.2}In_{37.2}Gd_{15.6}$	1/1	2.06	1.507 (0.5437)	0.216	0.3156
$Au_{49.7}In_{35.4}Ce_{14.9}$	1/1	2.01	1.528 (0.5526)	0.208	0.3142
$Au_{42.9}In_{41.9}Yb_{15.2}$	2/1	1.99	2.463 (0.5529)	0.223	0.3216
$Au_{42.9}In_{41.9}Ca_{14.5}$	2/1	1.99	2.477 (0.5562)	0.215	0.320
$Au_{64.4}Sn_{20.4}Ce_{15.2}$	1/1	1.92	1.521 (0.5526)	0.218	0.304
$Au_{64.2}Sn_{21.3}Pr_{14.5}$	1/1	1.93	1.516 (0.5508)	0.206	0.304
$Au_{60.7}Sn_{25.2}Eu_{14.1}$	1/1	1.90	1.535 (0.5574)	0.217	0.310
$Au_{62.3}Sn_{23.1}Gd_{14.6}$	1/1	1.99	1.497 (0.5437)	0.203	0.304
$Au_{61.2}Sn_{23.9}Dy_{14.9}$	1/1	2.02	1.490 (0.5414)	0.204	0.3031
Au–Sn–Tb	1/1	—	1.491	—	—
$Au_{61.2}Sn_{24.3}Ca_{14.5}$	2/1	1.87	2.437 (0.5472)	0.222	0.309
$Au_{61.2}Sn_{24.5}Eu_{14.3}$	2/1	1.88	2.487 (0.5584)	0.221	0.3106
$Au_{60.3}Sn_{24.6}Yb_{15.1}$	2/1	1.89	2.428 (0.5450)	0.229	0.3085
$Zn_{81}Mg_4Sc_{15}$	iQc	2.15	0.494	0.207	0.2872
$Zn_{77}Fe_7Sc_{16}$	iQc	2.09	0.497	0.226	0.2843

Table 1:1 Experimental (e/a) ratio for Ag-In-Gd approximant

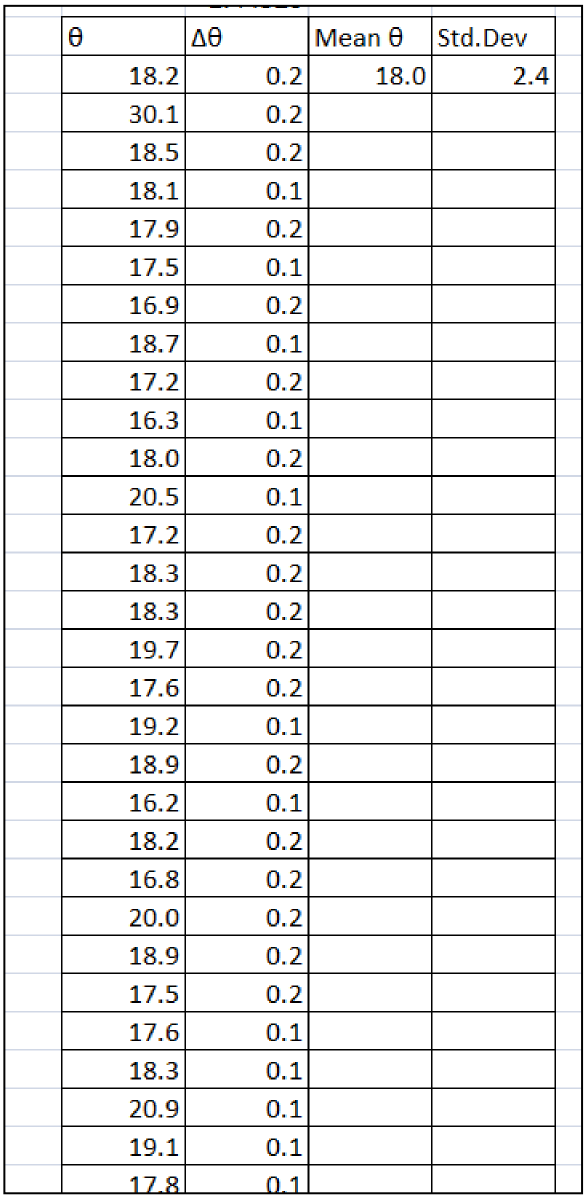

θ	Δθ	Mean θ	Std.Dev
18.2	0.2	18.0	2.4
30.1	0.2		
18.5	0.2		
18.1	0.1		
17.9	0.2		
17.5	0.1		
16.9	0.2		
18.7	0.1		
17.2	0.2		
16.3	0.1		
18.0	0.2		
20.5	0.1		
17.2	0.2		
18.3	0.2		
18.3	0.2		
19.7	0.2		
17.6	0.2		
19.2	0.1		
18.9	0.2		
16.2	0.1		
18.2	0.2		
16.8	0.2		
20.0	0.2		
18.9	0.2		
17.5	0.2		
17.6	0.1		
18.3	0.1		
20.9	0.1		
19.1	0.1		
17.8	0.1		

Table 2: Calculation of mean angle between (310) and (100) planes

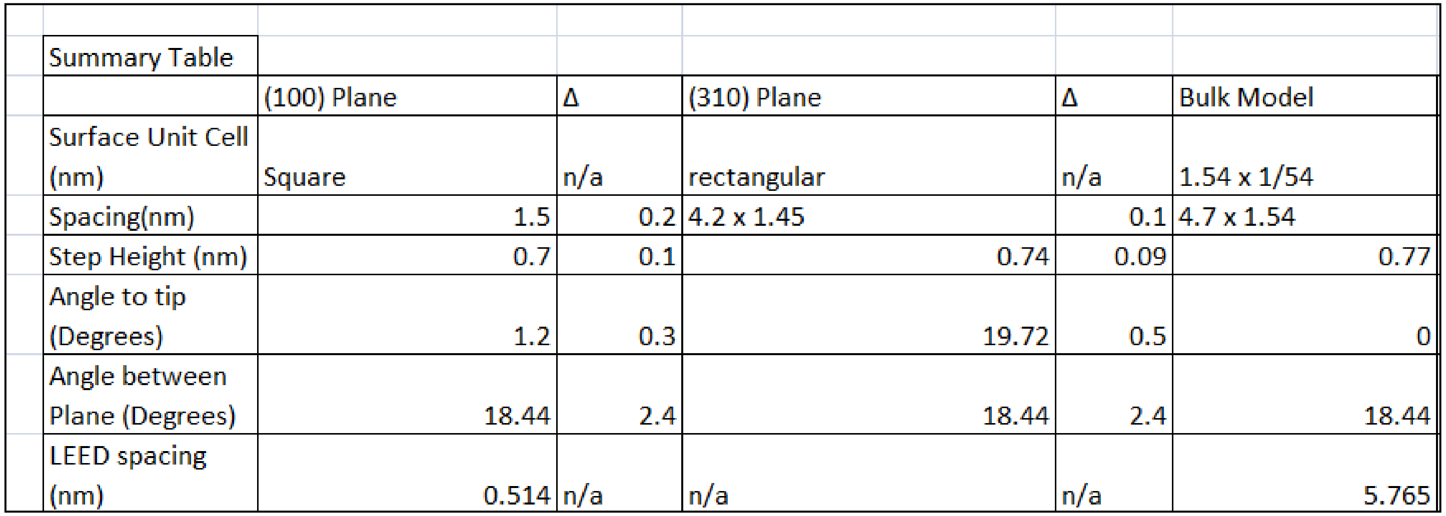

Summary Table					
	(100) Plane	Δ	(310) Plane	Δ	Bulk Model
Surface Unit Cell (nm)	Square	n/a	rectangular	n/a	1.54 x 1/54
Spacing(nm)	1.5	0.2	4.2 x 1.45	0.1	4.7 x 1.54
Step Height (nm)	0.7	0.1	0.74	0.09	0.77
Angle to tip (Degrees)	1.2	0.3	19.72	0.5	0
Angle between Plane (Degrees)	18.44	2.4	18.44	2.4	18.44
LEED spacing (nm)	0.514	n/a	n/a	n/a	5.765

Table 3: Summary of experimental findings compared with Bulk Model